https://doi.org/10.5194/egusphere-2026-2505
Preprint. Discussion started: 29 June 2026

Dynamic Satellite-Derived Vegetation and Radiation Inputs Advance Continental-Scale Hydrological Simulation Across China

Xinran Wu[1], Dawei Peng[1*], Xianhong Xie[1*], Yibing Wang[2], Arken Tursun[3], Yao Liu[1], Bowen Zhu[4], Cong Nie[1]

[1] State Key Laboratory of Remote Sensing and Digital Earth, Faculty of Geographical Science, Beijing Normal University, Beijing 100875, China

[2] Hubei Province Key Laboratory of Geographic Process Analysis and Simulation, Central China Normal University, Wuhan 430079, China

[3] State Key Laboratory of Ecological Safety and Sustainable Development in Arid Lands, Xinjiang Institute of Ecology and Geography, Chinese Academy of Sciences, Urumqi 830011, China

[4] College of Water Science and Engineering, Taiyuan University of Technology, Taiyuan 030024, China

* Corresponding authors: Dawei Peng (dawei_peng@mail.bnu.edu.cn)
Xianhong Xie (xianhong@bnu.edu.cn)

https://doi.org/10.5194/egusphere-2026-2505
Preprint. Discussion started: 29 June 2026

Abstract: Global vegetation greening is reshaping water and energy cycles, challenging land surface hydrological modeling. Satellite remote sensing provides dynamic observations of vegetation and radiation, offering a pathway to improve simulations. However, models often rely on static parameters, failing to capture critical transient biogeophysical feedbacks. This study quantifies the impact of integrating remote sensing data—leaf area index, fractional vegetation cover, albedo, and downward radiation—into the Variable Infiltration Capacity (VIC) model across China. We evaluated simulations against observed runoff from 50 stations, evapotranspiration (ET) from >40 flux sites, and satellite ET products. The dynamic data-driven VIC model accurately simulated runoff and ET. In ungauged basins, simple parameter transfer achieved Nash-Sutcliffe efficiency >0.6 for runoff. Using static vegetation parameters induced substantial biases: a national-scale ET underestimation of 5% (20 mm yr^{-1}) and runoff overestimation of 14% (29 mm yr^{-1}). In the rapidly greening basin (i.e., Pearl River Basin), dynamic vegetation data corrected ET and runoff biases by ~70 mm yr^{-1}. Remote sensing radiation data offered limited improvement, likely due to the model's inherent radiation estimation capability. This work provides conclusive evidence that dynamic remote sensing data, particularly vegetation parameters, are crucial for accurate large-scale hydrological simulation in changing environments, offering a practical framework for data-sparse regions.

Keywords: Land surface model; Continental-scale simulation; Remote sensing products; Dynamic vegetation; Radiation; Runoff; Evapotranspiration

https://doi.org/10.5194/egusphere-2026-2505
Preprint. Discussion started: 29 June 2026

1. Introduction

Over recent decades, widespread greening of terrestrial vegetation has markedly altered land–atmosphere exchanges of water and energy (Alkama et al. 2022; Piao et al. 2020; Zhao et al. 2022). Greening increases transpiring leaf area and canopy conductance, which can enhance evapotranspiration (ET) (Jiang et al. 2022; Peng et al. 2024). Meanwhile, vegetation expansion, particularly forest gain, often reduces surface albedo, increasing absorbed solar radiation and further intensifying the water cycle (Duveiller et al. 2018; Findell et al. 2017). Vegetation also reshapes hydrologic partitioning through canopy interception, litter effects, and root activity, thereby modifying precipitation redistribution, infiltration conditions, and soil water storage and regulation (Rajão et al. 2023; Tang et al. 2025). These changes, in turn, affect the timing and magnitude of surface runoff and groundwater recharge (Liu et al. 2025b; Yan et al. 2024b). Vegetation dynamic has introduced significant challenges for land surface models (LSMs), which must now accurately represent these transient biogeophysical feedbacks to reliably simulate terrestrial water and energy budgets under changing conditions. Consequently, adapting LSMs to capture the dynamic effects of vegetation change has emerged as a critical and timely research focus in modern hydrology and Earth system science.

Since the 1980s, LSMs have undergone three major iterations (Pitman 2003; Sato et al. 2014; Singh 2018). First-generation LSMs used fixed land surface conditions and coupled simple energy and water balance processes for simulation (Sellers et al. 1986), such as the Biosphere-Atmosphere Transfer Scheme (BATS) model developed by Dickinson (1986). These models did not simulate key components such as vegetation dynamics, or the carbon cycle and contained significant uncertainties (Sato et al. 2014). For instance, their simplistic representation of the land surface

https://doi.org/10.5194/egusphere-2026-2505
Preprint. Discussion started: 29 June 2026

failed to capture real-world complexity, and their hydrological processes often relied on the Manabe bucket model (Manabe 1969), resulting in a single runoff generation mechanism. Building upon first-generation models, second-generation LSMs were rapidly developed. Compared to their predecessors, they accounted for spatial heterogeneity in land surface conditions and offered a more comprehensive representation of energy and water balances, incorporating vegetation effects on energy balance and multiple runoff generation mechanisms (Pitman 2003; Sato et al. 2014). Describing the influence of vegetation status on water and energy balances was a key advancement in this generation.

Third-generation LSMs further refined the description of vegetation physiological mechanisms within the models and incorporated simulations of the carbon cycle (Lombardozzi et al. 2015). Several prominent land surface models emerged during this period, including the Community Land Model (CLM) (Bonan et al. 2002), the Variable Infiltration Capacity (VIC) model (Liang et al. 1994), and the Noah multi-parameterization (Noah-MP) model (Niu et al. 2011). The development of these models enabled the simulation of more detailed land surface processes, such as ET components and gross primary productivity (GPP), significantly enhancing the simulation capability and accuracy of LSMs and achieving more comprehensive coupling of various physical and physiological mechanisms (Bohn et al. 2013; Lawrence et al. 2019). Consequently, with well-developed physical mechanisms, providing accurate parameters and data to the models has become key to achieving their optimal performance.

LSM performance depends strongly on parameterization and on the extent to which inputs represent evolving climate and land surface conditions (Brekke et al. 2014; Shi et al. 2021; Silwimba et al. 2025; Yan et al. 2021; Zhao et al. 2025). Vegetation is commonly represented in

https://doi.org/10.5194/egusphere-2026-2505
Preprint. Discussion started: 29 June 2026

LSMs in two ways. One approach utilizes an internal dynamic vegetation module, as implemented in CLM and Noah-MP (Bonan and Levis 2006; Niu et al. 2011). The strength of this method is its ability to capture long-term vegetation succession and associated ecohydrological feedbacks. However, it increases model complexity and parameter dimensionality, raising computational and calibration costs and amplifying uncertainty through reduced parameter identifiability (Arsenault et al. 2018). Remote-sensing products are therefore commonly used to constrain and calibrate key states and parameters, with independent data used for validation. (Huo et al. 2024; Raoult et al. 2025). A second approach prescribes time varying vegetation parameters from remote sensing directly within the LSM, as in VIC (Bohn and Vivoni 2016). Advances in multispectral, hyperspectral, and active microwave sensors have expanded the availability of remote sensing vegetation and radiation products. Improved retrieval algorithms and data assimilation further enhance these datasets (Liang et al. 2021; Liang et al. 2013; Yan et al. 2024a). These include refined vegetation structural metrics, such as Leaf Area Index (LAI), Fractional Vegetation Cover (FVC), and albedo (Cao et al. 2023; Dong et al. 2025), and improved estimates of surface radiation components, including downward shortwave (Rs) and downward longwave (Rl) radiation (Cheng and Liang 2016; Guo et al. 2018). At regional scales, these products provide an effective way to characterize vegetation and radiation dynamics and support LSM representation of vegetation change and the surface energy balance (de Ávila et al. 2023; Peng et al. 2024). However, the extent to which these vegetation and radiation forcings affect LSM simulations of hydrologic processes remains unclear.

In this study, we employ the VIC model, a well-established land surface model renowned for its robust representation of the water and energy balance. We drive the model with remote sensing-

https://doi.org/10.5194/egusphere-2026-2505
Preprint. Discussion started: 29 June 2026

derived dynamic vegetation and radiation parameters to quantify their impacts on hydrological simulations. To rigorously evaluate this dynamic data-driven approach at a continental scale, we focus on the region of China. This region is characterized by significant vegetation greening and encompasses a wide spectrum of climatic and vegetative regimes—from arid to humid zones, providing an ideal testbed. The model is first calibrated and validated against multi-source observational data. Through a series of carefully designed scenario experiments, we then isolate and quantify the individual effects of dynamic vegetation and dynamic radiation parameters on key hydrological processes. This work aims to provide concrete guidance for the effective integration of satellite remote sensing products into land surface modeling, thereby advancing the accuracy of large-scale hydrological flux simulations in a changing environment.

2. Data and methods

2.1. Description of the VIC model

The VIC model (version 4.2.d used in this study) divides the study area into regular grid cells and further subdivides each grid into multiple hydrological response units based on land cover types (Liang et al. 1994). It simulates both the water balance (e.g., runoff, ET) and the energy balance (e.g., sensible and latent heat fluxes, H and LE) at the grid scale. Currently, the VIC model, as one of the representative LSMs, is widely used for hydrological analysis at regional and global scales (Jiang et al. 2022; Peng et al. 2024; Shrestha et al. 2025).

https://doi.org/10.5194/egusphere-2026-2505
Preprint. Discussion started: 29 June 2026

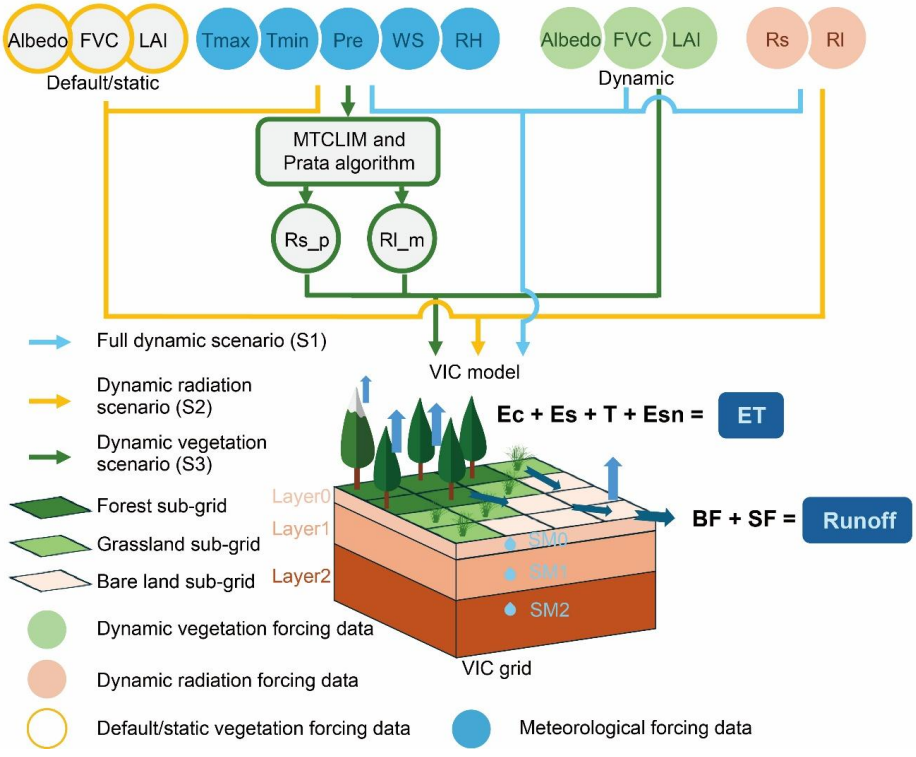

Fig. 1. Schematic diagram of the VIC model. In the figure, default/static Albedo, FVC, and LAI represent multi-year average monthly data. Tmax, Tmin, Pre, WS, and RH denote maximum temperature, minimum temperature, precipitation, wind speed, and relative humidity, respectively. Rs and Rl represent shortwave radiation and longwave radiation, with Rs_p and Rl_m indicating Rs calculated by the Prata algorithm and Rl calculated by MTCLIM, respectively. Ec denotes canopy interception evaporation, Es is soil evaporation, T represents transpiration, and Esn signifies snow/ice sublimation. BF and SF refer to baseflow and surface runoff, respectively. Layer 0, 1, and 2 indicate the three soil layers. SM 0, 1, and 2 represent the soil moisture content for the three soil layers.

For the ET simulation (Fig. 1), the VIC model computes ET within a water-balance framework, partitioning it into soil evaporation (Es), evaporation of intercepted water from the vegetation canopy (Ec), vegetation transpiration (T), and snow/ice sublimation (Esn). Total ET is calculated as the follows equation:

$$\mathrm{ET} = \int_{n=1}^{N} \mathrm{FVC}_n \times (\mathrm{Ec} + \mathrm{T}) + FVC_{N+1}\mathrm{Es} + \mathrm{Esn} \quad (1)$$

where, FVC_n is the FVC for each vegetation type, FVC_{N+1} is the area of bare soil. Note that, by default/static, FVC is prescribed as a static value and is set to 1 within the vegetation sub-grid,

https://doi.org/10.5194/egusphere-2026-2505
Preprint. Discussion started: 29 June 2026

implying full vegetation cover (Fig. 1). After introducing dynamic vegetation data, this value is replaced with the daily FVC. The equation for the three main ET components (Ec, T and Es) are as follows:

$$\mathrm{Ec} = f\left(\frac{W_i}{K_L \times \mathrm{LAI}}\right)^{\frac{2}{3}} \frac{r_w}{r_w + r_0} \mathrm{PET} \quad (2)$$

where, f is the fraction of the time step during which evaporation from canopy interception occurs, W_i represents the intercepted water storage within the vegetation canopy, K_L is a constant, typically set to 0.2; the LAI used here, if no dynamic vegetation data are provided, is the multi-year monthly average LAI value. r_w denotes the resistance coefficient for water evaporation, r_0 is the surface evaporation resistance, and PET represents potential evaporation.

T is calculated using the following equation:

$$\mathrm{T} = (1-f)\frac{r_w}{r_w + r_0 + r_c}\mathrm{PET} + f\left[1 - \left(\frac{W_i}{K_L \times \mathrm{LAI}}\right)^{\frac{2}{3}}\right]\frac{r_w}{r_w + r_0 + r_c}\mathrm{PET} \quad (3)$$

where, r_c is the canopy resistance (S m−1).

Es is assumed to originate from layer 0, the surface soil layer (typically 0.1 m thick). The VIC model represents the effects of soil heterogeneity on Es using a variable infiltration capacity curve. Evaporation is further limited by water availability, such that Es does not exceed the available liquid water in the soil profile and remains consistent with the water balance. Together with the energy balance constraint used to compute PET, Es is estimated subject to these constraints and can be written as:

$$\mathrm{Es} = \mathrm{PET} \times A_s + (1 - A_s) \times \left(1 - A^{1/b_i}\right) \times 1 + \sum_{n=1}^{30} \frac{b_i \times A^n}{b_{i+n}} \quad (4)$$

where, A_s denotes the areal fraction corresponding to when the water content in bare soil reaches the saturation condition. b_i defines the shape of the variable infiltration capacity curve. A is the proportion of soil within the grid that has reached saturation (0-1). When $A_s = 1$, $\mathrm{Es} = \mathrm{PET}$. If

https://doi.org/10.5194/egusphere-2026-2505
Preprint. Discussion started: 29 June 2026

Es > 0 and the SM0 (layer0 soil moisture, mm), then Es $= 0$.

In the runoff simulation, VIC computes surface runoff (SF) and baseflow (BF) separately. SF is primarily constrained by infiltration in the upper soil layer, whereas BF is mainly controlled by SM (Soil moisture) in the bottom layer. SF is computed under two cases. The first case applies when the top soil layer is fully saturated and is calculated as:

$$\mathrm{SF} = Pre - (SM0_{max} - SM0) \tag{5}$$

where, $SM0_{max}$ is the maximum moisture content of layer0 (mm) .When the layer0 is partially saturated, the calculation method is as follows:

$$\mathrm{SF} = Pre - \left(SM_{0,max} - SM_0\right) + SM_{0,max} \times \left(1 - \frac{i+Pre}{i_m}\right)^{1+b_i} \tag{6}$$

where, i_m is the maximum infiltration capacity (mm). For BF, the calculation method is as follows:

$$\mathrm{BF} = \begin{cases} \frac{D_s \times D_{smax}}{W_s} \times SM_r & SM_r > W_s \\ \frac{D_s \times D_{smax}}{W_s} \times SM_r + D_{smax} \times \left(1 - \frac{D_s}{W_s}\right) \times \left(\frac{SM_r - W_s}{1 - W_s}\right)^c & SM_r > W_s \end{cases} \tag{7}$$

where, D_s is the baseflow coefficient for the saturated zone, D_{smax} is the maximum baseflow velocity (mm day^{-1}), SM_r is the relative SM, W_s is the SM threshold at which nonlinear baseflow begins. Among these, D_s, D_{smax}, and W_s are input parameters that require calibration.

Note that most previous VIC applications prescribe static vegetation parameters (Meng et al. 2020; Xie et al. 2015; Zhu et al. 2021). In this study as shown in Fig. 1, we force VIC with remotely sensed dynamic vegetation (LAI, FVC and albedo) parameters and radiation (Rs and Rl) forcings to better represent hydrologic processes and water fluxes. We run the model at a 3 h time step to guarantee water and energy balance. The 3-h simulated outputs are aggregated to daily values for 2000–2020, with 1995–1999 used as a spin-up period. The simulations are conducted at 0.0625°

https://doi.org/10.5194/egusphere-2026-2505
Preprint. Discussion started: 29 June 2026

spatial resolution, covering 246,029 grid cells across China.

2.2. Model input data

2.2.1. Basic driver data for the model

The input data for the VIC model include meteorological forcing, soil parameters, topographic information, vegetation parameters. The gridded meteorological forcing is taken from the spatiotemporal interpolation of station observations used in previous studies (Jiang et al. 2022; Peng et al. 2024; Xie et al. 2015; Zhu et al. 2021). It includes daily 0.0625° Pre, Tmax, Tmin, WS, and RH. The digital elevation model (DEM) data were obtained from the SRTM dataset provided by the United States Geological Survey (https://earthexplorer.usgs.gov/) at a spatial resolution of 90 m. This dataset was used not only to drive the VIC model but also to delineate watershed catchments and serve as an auxiliary variable in the interpolation of meteorological data.

The VIC model describes land surface conditions through soil parameter files, a vegetation library, and vegetation parameter files. The soil parameter file primarily provides physical and chemical properties related to soil, such as soil type and thickness. We referred to the Chinese Soil Map for soil type distribution and obtained parameters for each soil layer, including saturated hydraulic conductivity, bulk density, and field capacity, from existing research (Shangguan et al. 2013; Wang et al. 2024; Zhu et al. 2021). Parameters such as bare soil surface roughness and thermal damping depth were derived from Nijssen et al. (2001).

The vegetation library file contains parameters for all vegetation types considered in the model, all referenced from the official VIC model documentation (https://vic.readthedocs.io/en/vic.4.2.d/). The vegetation parameter file describes the composition and structural characteristics of vegetation within each grid cell, including the number of

https://doi.org/10.5194/egusphere-2026-2505
Preprint. Discussion started: 29 June 2026

vegetation types, the fractional coverage of each type, and root depth and distribution. We used land cover data generated from Landsat TM imagery at a spatial resolution of 1 km. To ensure the input data reflect relatively stable vegetation patterns, the land cover data for the year 2010 were selected for this study.

2.2.2. Remote sensing-based parameters and forcings

In addition to its basic parameter set, the VIC model can be driven by time-varying remote sensing inputs. These include dynamic vegetation parameters—specifically LAI, FVC, and surface albedo—and radiation forcings comprising Rs and Rl. The dynamic vegetation inputs replace the model's default monthly climatological values, which are normally prescribed as long-term averages over the study period. The vegetation parameters were obtained from the Global LAnd Surface Satellite (GLASS, https://www.geodata.cn) product (Liang et al. 2021). This dataset provides global coverage with an 8-day temporal resolution and a 500-meter spatial resolution. The LAI and FVC data were respectively retrieved from MODIS and Landsat/MODIS observations using general regression neural networks (Jia et al. 2016; Xiao et al. 2014). The surface albedo product was generated from multi-angle observations with statistical temporal filtering (Liu et al. 2013). All 8-day composite datasets were linearly interpolated to a daily temporal resolution and spatially resampled to a 1-km grid to align with the land cover data.

The VIC model typically estimates surface radiation fluxes internally using the MTCLIM and Prata algorithms, which derive these fluxes indirectly from standard meteorological inputs such as air temperature and humidity. In this study, we replace these internal estimates by directly incorporating remote sensing radiation products as model forcings. Specifically, the Rs is obtained from the GLASS product, which is generated using a direct estimation method that converts

https://doi.org/10.5194/egusphere-2026-2505
Preprint. Discussion started: 29 June 2026

MODIS top-of-atmosphere reflectance via a radiative transfer model (Zhang et al. 2014). The Rl is sourced from a high-accuracy fusion product (He et al. 2020), available through the National Tibetan Plateau Data Center (https://data.tpdc.ac.cn). This product integrates ground observations, remote sensing, and reanalysis data at an original spatiotemporal resolution of 0.1° and 3-hourly. Both Rs and Rl datasets were spatially resampled to the model's 0.0625° grid and temporally interpolated to a daily resolution.

2.3. Model evaluation data

2.3.1. In-situ observations of streamflow and ET

To calibrate and validate model parameters, we compile streamflow and ET observations across China. For streamflow, we collect records from 50 gauging stations and convert discharge to runoff by normalizing by the corresponding basin area (Tab. S1). These stations span China's nine major river basins (Fig. 2b): 14 in the Yangtze River Basin (Yz. RB), 8 in the Yellow River Basin (Ye. RB), 4 in the Huaihe River Basin (Huai. RB), 4 in the Haihe River Basin (Hai. RB), 6 in the Pearl River Basin (Pe. RB), 4 in the Songliao River Basin (SL RB), 5 in the Southeast Rivers Basin (SE RB), 3 in the Interior Rivers Basin (In. RB), and 2 in the Southwest Rivers Basin (SW RB). Runoff for six stations (Lijiadu, Hushan, Wanjiabu, Dufengkeng, Changdu, and Nuxia) is taken from the Annual Hydrological Report for P.R.C. Data for seven stations (Zhangjiashan, Zhuangtou, Huaxian, Heishiguan, Wuzhi, Baimasi, and Xianyang) are obtained from the National Earth System Science Data Center – Loess Plateau Sub-center (http://loess.geodata.cn). All remaining stations are from the China River Sediment Bulletin (http://www.mwr.gov.cn/). To evaluate nationwide parameter transfer, we use 41 basins for calibration and validation and reserve 9 basins for an independent assessment of transferability.

https://doi.org/10.5194/egusphere-2026-2505
Preprint. Discussion started: 29 June 2026

ET observations are compiled from multiple networks, including 18 sites from FLUXNET (https://fluxnet.org/), 12 sites from ChinaFLUX (https://chinaflux.org/), and 11 sites from the Heihe Watershed Allied Telemetry Experimental Research (HiWATER, https://data.tpdc.ac.cn/), for a total of 41 sites (Fig. 2a, Tab. S2). Flux measurements are generally interpreted as representative of land surface energy exchange over an approximately 1 km footprint. To reduce representativeness mismatch, we validate the model at the corresponding sub-grid scale.

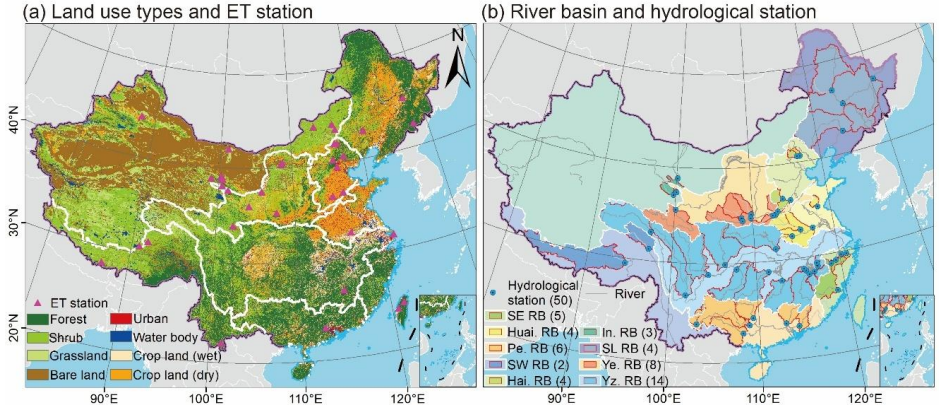

Fig. 2. (a) Land cover classification and spatial distribution of ET observation sites across China; (b) spatial distribution of hydrological stations and their controlled sub-basins. The white lines on the map represent the boundaries of the nine major river basins.

2.3.2. Remote sensing based ET products

Recognizing that site-scale validation alone is insufficient to assess the spatial performance of model simulations, we compile four widely used ET products for evaluation: the Global Land Evaporation Amsterdam Model (GLEAM), Penman Monteith Leuning V2 China (PML), GLASS, and ETMonitor. The GLEAM product is developed by Vrije Universiteit Amsterdam (https://www.gleam.eu/). I It has a 0.1° spatial resolution and daily temporal resolution. GLEAM v4.1a computes potential evaporation using a modified Penman equation, and then converts it to actual ET by applying an evaporation stress factor constrained by multi-source satellite

https://doi.org/10.5194/egusphere-2026-2505
Preprint. Discussion started: 29 June 2026

observations, including microwave vegetation optical depth, vapor pressure deficit, and SM (Miralles et al. 2025).

The PML dataset is provided by the National Tibetan Plateau Data Center (https://www.tpdc.ac.cn). This dataset is generated using a modified Penman Monteith Leuning model that couples vegetation transpiration to photosynthetic assimilation through a stomatal conductance scheme (Zhang et al. 2019; Zhang et al. 2016). The model uses MODIS-derived inputs, including land surface reflectance, LAI, and dynamic vegetation type, enabling robust upscaling from site to regional scales. The product has a 500 m spatial resolution and daily temporal resolution.

The GLASS land surface LE product integrates multi-source remote sensing information and applies Bayesian averaging to combine five ET estimation algorithms, improving robustness and accuracy (Liang et al. 2013; Yao et al. 2015; Yao et al. 2014; Zhao et al. 2013). The fusion scheme optimizes algorithm weights across land cover types and uses AVHRR, MODIS, and MERRA reanalysis data to produce a global LE product at 0.05° spatial resolution and 8-day temporal resolution. After acquisition, LE is converted to ET using a standard conversion relationship.

The ETMonitor global 1-km land surface actual ET dataset is provided by the National Tibetan Plateau Data Center (https://data.tpdc.ac.cn). It is produced by the ETMonitor model using multi-source remote sensing and reanalysis inputs, including MODIS land cover and snow cover, ESA CCI SM, GLASS LAI, FVC, and albedo products, and ERA5 atmospheric reanalysis. The dataset is evaluated against 251 global flux towers and shows high accuracy (Zheng et al. 2022).

https://doi.org/10.5194/egusphere-2026-2505
Preprint. Discussion started: 29 June 2026

2.4. Parameter estimation

The application of VIC requires parameter calibration, followed by validation of the simulation reliability during the validation period. The study by Zhu et al. (2021) has ever well calibrated the VIC model parameters over China, so here we took their parameter values as default estimates and performed calibration, validation, and parameter transfer for the scenario incorporating the newly added vegetation and radiation dynamic data.

The seven calibrated parameters include the soil layer depths (D_1, D_2, D_3), three baseflow parameters (D_s W_s, D_{smax}) and b_i (Nijssen et al. 2001). We identify the optimal parameter set through iterative calibration by testing parameter combinations to improve agreement with observed hydrologic behavior. Calibration typically starts with the three soil layer depths, which are first assigned based on local soil properties. The top layer depth $(D_1)$is usually prescribed as a thin surface layer (0.1 m), and adjustments mainly target $D_2$and D_3. We then tune the three baseflow parameters. D_{smax} is the maximum baseflow velocity for each grid cell and can be approximated as saturated hydraulic conductivity $(Ksat)$multiplied by grid slope. The initial value of W_s is typically set to 0.9 and defines the SM threshold at which nonlinear baseflow initiates. $D_s$represents the fraction of D_{smax}at which nonlinear baseflow starts, with an initial value of 0.0001 and generally less than 1. Finally, we adjust b_i, the shape parameter of the Variable Infiltration Curve and a defining feature of VIC. Typical $b_i$values range from 10^{-5} to 0.4, with an initial value of 0.2. Larger $b_i$reduces peak flow and decreases runoff generation. Calibration and validation are conducted for 41 sub-basins spanning China's nine major river basins. The calibrated parameters are then related to multi-year mean meteorological variables (Pre, mean temperature, RH), radiation (Rs), and vegetation (LAI and FVC) using multiple linear regression

https://doi.org/10.5194/egusphere-2026-2505
Preprint. Discussion started: 29 June 2026

(MLR). The resulting MLR models are evaluated in nine uncalibrated sub-basins and are used to transfer parameters to ungauged basins. The MLR model is expressed as follows:

$$y_k = \beta_{0,k} + \beta_{1,k}Pre + \beta_{2,k}Tem + \beta_{3,k}RH + \beta_{4,k}Rs + \beta_{5,k}LAI + \beta_{6,k}FVC + \epsilon_k \quad (8)$$

where, y_k is the kth hydrological parameter requiring calibration (b_i, D_s, D_{smax}, W_s, D_1, D_2, D_3). $\beta_{0,k}$ is the intercept for the kth dependent variable. $\beta_{1,k}$, $\beta_{2,k}$, $\beta_{3,k}$, $\beta_{4,k}$, $\beta_{5,k}$, and $\beta_{6,k}$ are the regression coefficients corresponding to the kth dependent variable. ϵ_k is the error term for the kth dependent variable.

2.5. Model scenario design

To quantify the separate effects of the dynamic vegetation and the radiation forcings on simulated water fluxes, we design three experiments (Fig. 1; Tab. 1). In S1, VIC is forced with daily dynamic vegetation parameters and radiation forcings. In S2, VIC uses dynamic radiation but retains the default static vegetation. In S3, VIC uses dynamic vegetation but retains the default radiation estimated from meteorological inputs. We isolate the effects of dynamic vegetation and dynamic radiation on runoff and ET as the differences between S1 and S2, and between S1 and S3, respectively.

Tab. 1. Dynamic parameters and forcings used in different scenarios to detect their effects on water flux simulations

Scenario	LAI	FVC	Albedo	Rs	Rl	Purpose
S1	Dynamic	Dynamic	Dynamic	Dynamic	Dynamic	Baseline simulation with fully dynamic parameter.
S2	Default/ static	Default/ static	Default/ static	Dynamic	Dynamic	Using the default/static vegetation forcing, S2-S1 = the effect of dynamic vegetation parameter.
S3	Dynamic	Dynamic	Dynamic	Default (Rs_m)	Default (Rl_p)	Using the default radiation forcing, S3-S1 = the effect of dynamic radiation parameter.

https://doi.org/10.5194/egusphere-2026-2505
Preprint. Discussion started: 29 June 2026

3. Results

3.1. Model parameter calibration, validation, and transfer

3.1.1. Parameter calibration and validation

After incorporating dynamic vegetation and radiation data into the VIC model, we calibrated and validated its parameters using observed runoff data from the 41 hydrological stations. Model performance was assessed using four standard metrics: the Pearson correlation coefficient (R), the Nash-Sutcliffe efficiency (NSE), the Kling-Gupta efficiency (KGE), and the relative bias (Bias). During the calibration period (Figs. 3a-d, Table S3), the multi-basin average values for these metrics are R = 0.88, NSE = 0.73, KGE = 0.71, and Bias = 5.05%. Spatially, the model performs well in southern and eastern China, including the Yz. RB, Pe. RB, and SE RB. Model performance is markedly weaker in northern and northeastern China, such as in the SL RB and Hai. RB, as indicated by relatively lower NSE and KGE values. Additionally, substantial underestimation occurs in the southwestern region of China (SW RB), while clear overestimation is observed in the source area of the Yangtze River. During the validation period, model performance shows a slight decline, with multi-basin metrics of R = 0.86, NSE = 0.68, KGE = 0.71, and Bias = –0.08%. The spatial pattern of model performance in the validation period is similar to that observed during the calibration period.

Among the 12 representative sub-basins, the VIC model effectively captures the seasonal and interannual variations in runoff (Figs. 3i-t). The model performs well during both the calibration and validation periods in three sub-basins in the Yz. RB (Beibei, Xiangtan, Hushan), two stations in the Ye. RB (Huaxian and Wuzhi), the Shijiao station in the Pe. RB, and the Zhuji station in the SW RB (Figs. 3i-m, p and r). In these sub-basins, the *R* value exceeds 0.85, the *NSE* and *KGE*

https://doi.org/10.5194/egusphere-2026-2505
Preprint. Discussion started: 29 June 2026

values are above 0.65, and the *Bias* remains within 10% for both periods. In contrast, the *NSE* and *KGE* for simulated runoff at Jiamusi in the SL RB are relatively low, both falling below 0.6 during the calibration period (Fig. 3q). At Buhahekou in the In. RB, the *Bias* shows a substantial increase during the validation period compared to the calibration period (Fig. 3s). The VIC model exhibits larger biases in runoff simulation for Linyi in the Huai. RB and Nuxia in the SW RB. Linyi shows overestimation, with an average *Bias* of 25.88% during calibration and 29.51% during validation (Fig. 3n). Nuxia shows underestimation, with a *Bias* of –35.83% during calibration and –26.87% during validation (Fig. 3t).

https://doi.org/10.5194/egusphere-2026-2505
Preprint. Discussion started: 29 June 2026

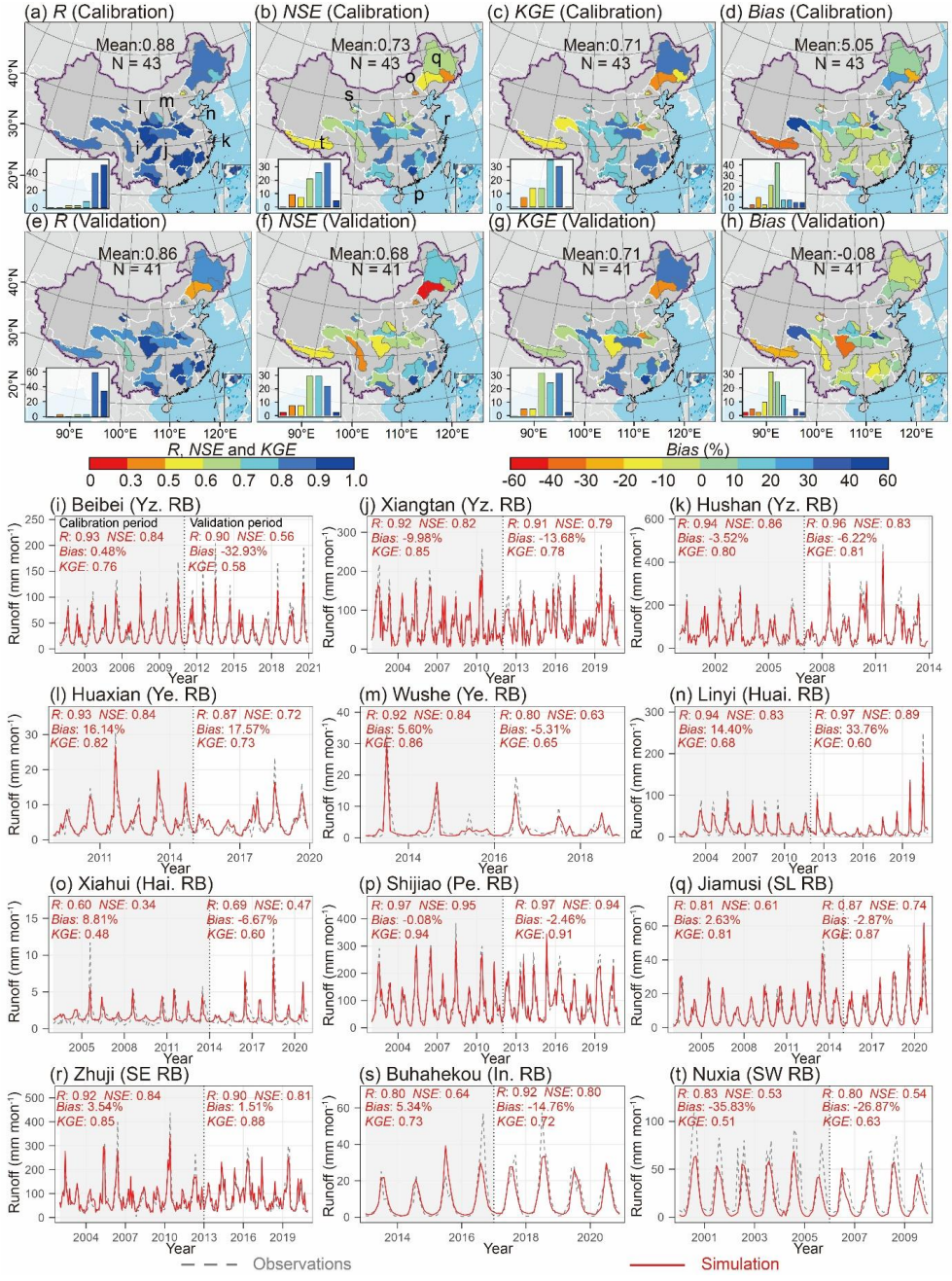

Fig. 3. Spatial distribution of *R*, *NSE*, *KGE*, and *Bias* for the VIC model during the (a–d) calibration period and (e–h) validation period, along with the specific simulation accuracy for (i–t) 12 representative sub-basins. The histograms in panels a–h show the frequency distribution, representing the percentage of the total number in each color segment. In panels i–t, the gray-shaded areas indicate the calibration period, and the white areas indicate the validation period. In panels a and b, the letter labels indicate the spatial locations of the sub-basins

https://doi.org/10.5194/egusphere-2026-2505
Preprint. Discussion started: 29 June 2026

presented in panels i–t.

3.1.2. Evaluation in ungauged basins

To transfer the calibrated parameters to ungauged regions, we applied a multiple linear regression method and validated the transfer performance using nine watershed stations that were not involved in calibration. As shown in Fig. 4, the VIC model with default parameters generally captures the pattern of runoff, with a mean *R* of 0.89 across the 9 basins (Fig. 4j). However, under this parameter setting, *NSE* and *KGE* are relatively low and *Bias* is high. The average *NSE* and *KGE* are 0.51 and 0.44, respectively, and the average |*Bias*| is 30.56% (Fig. 4j). Specifically, for the nine basins, the VIC model with default parameters tends to considerably underestimate runoff, with an average *Bias* of –29.10% (Figs. 4a–i).

Following parameter transfer via the multiple linear regression method, the VIC model achieves mean performance metrics of R = 0.90, NSE = 0.74, KGE = 0.68, and |Bias| = 10.63% across the nine validation basins (Fig. 4j). Compared to the simulations using default parameters, the transferred parameters lead to significant improvement in runoff simulation accuracy, corresponding to relative increases of 12.50% in R, 45.10% in NSE, 54.55% in KGE, and a decrease of 65.22% in |Bias|. In detail across the nine basins, the VIC model shows slight underestimation in six basins (Figs. 4d–i), with only the Gaochang station having a Bias less than –20% (–26.01%, Fig. 4h).

https://doi.org/10.5194/egusphere-2026-2505
Preprint. Discussion started: 29 June 2026

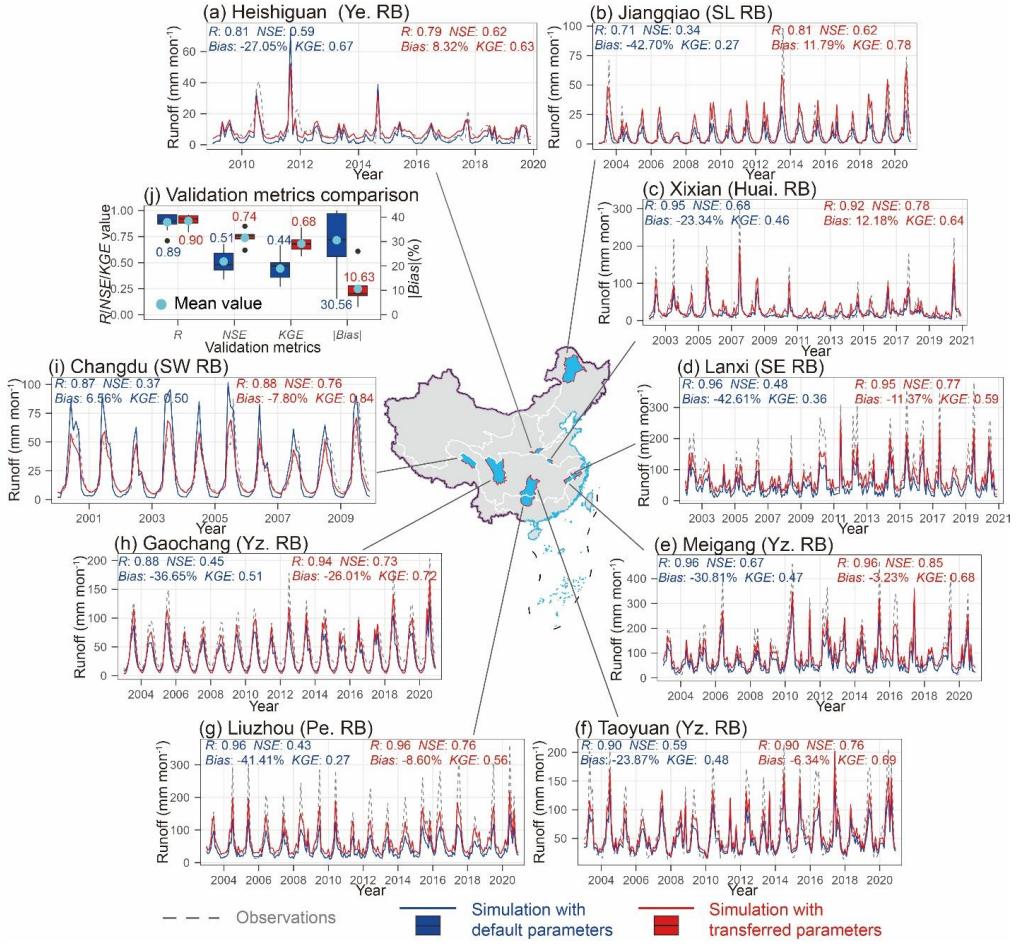

Fig. 4. (a–i) Individual accuracy comparison of simulated runoff between the parameter transfer method and default parameters across 9 sub-basins, and (j) an overall performance comparison.

3.2. Validation of model-simulated ET

We validate the ET simulated by the calibrated and parameter-transferred VIC model against in-situ observations from the 41 flux tower sites. The results indicate a mean R of 0.61 between the simulated and observed ET across all sites, with approximately half of the sites (51%) exhibiting an R value greater than 0.6 (Fig. 5a). The mean RMSE is 1.99 mm day^{-1}, and nearly half of the sites (49%) have an RMSE below 1.50 mm day^{-1} (Fig. 5b). The mean Bias is –39.41%,

https://doi.org/10.5194/egusphere-2026-2505
Preprint. Discussion started: 29 June 2026

and the absolute Bias is within 20% for roughly half (46%) of the sites (Fig. 5c). Spatially, the VIC-simulated ET shows a tendency towards underestimation in northern China and overestimation in northeastern China.

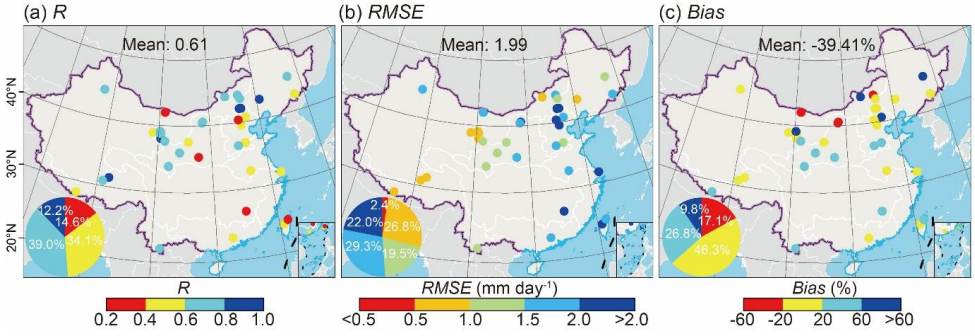

Fig. 5. Spatial distribution of (a) *R*, (b) *RMSE*, and (c) *Bias* for the comparison between VIC-simulated ET and site-observed ET.

We further validate the simulated ET by comparing it with the established four satellite-derived ET products: GLEAM, PML, GLASS, and ETMonitor. The VIC-simulated ET exhibits strong spatial consistency with all four products, all consistently capturing the characteristic northwest-to-southeast increasing gradient across China (Figs. 6a–e). In terms of the national multi-year mean, the VIC simulation yields a value of 393.83 mm yr^{-1}, which falls within the range spanned by the four products (387 to 439 mm yr^{-1}). This agreement is also evident at the scale of the nine major river basins in China (Fig. 6f). The temporal dynamics are equally well represented, with the monthly time series of VIC-simulated ET showing high correlation coefficients ($R > 0.97$) with all four products (Fig. 6g). The relative difference is less than 5% when compared to the PML and GLASS products, and approximately –8% to –10% against GLEAM and ETMonitor. These results demonstrate that the VIC model, when driven by dynamic remote sensing data, produces ET estimates that are highly comparable to multiple independent satellite-based products, and reliably captures the spatiotemporal dynamics of ET at the continental scale.

https://doi.org/10.5194/egusphere-2026-2505
Preprint. Discussion started: 29 June 2026

VIC-simulated ET over China increases from the northwest to the southeast (Fig. 6a), consistent with the spatial patterns in the reference products (Figs. 6b–e). The national mean ET from VIC is 393.83 mm yr^{-1}, which lies in the mid-range of the products, lower than ETMonitor, GLEAM, and GLASS but higher than PML (Figs. 6b–e). Across river basins (Fig. 6f), VIC closely matches the product means, with no consistent over- or underestimation in any basin. VIC also reproduces the observed temporal increase in ET over 2000–2020 ($p < 0.01$) (Fig. 6g). The ET trend from VIC is 0.23 mm mon^{-1}, intermediate among the products and comparable to the ET from GLASS. The comparison yields a mean R of 0.99 and a mean difference of –5.30%.

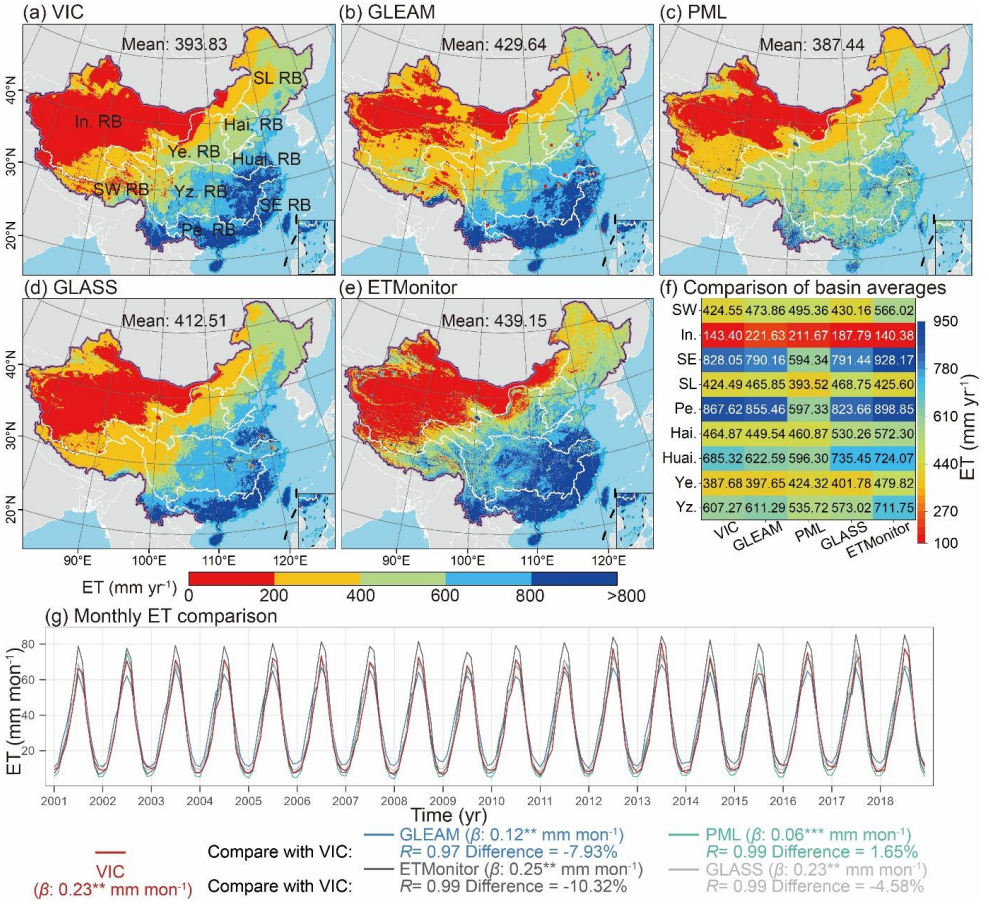

Fig. 6. Comparison of (a–d) spatial distribution, (e)mean values across different river basins, and (f) monthly

https://doi.org/10.5194/egusphere-2026-2505
Preprint. Discussion started: 29 June 2026

trends among VIC-simulated ET, GLEAM, PML, GLASS, and ETMonitor. β indicates the temporal trend of the variable, **indicates that the p-value for the slope is less than 0.01, and ***indicates $p < 0.001$.

3.3. Impact of remote sensing data on model-simulated ET

We assess the sensitivity of VIC-simulated ET to dynamic vegetation parameters and radiative forcing using the experimental scenarios outlined in Table 1. Neglecting vegetation dynamics (i.e., using static vegetation data) leads to a national mean ET reduction of 5.11% (20.08 mm yr^{-1}) (Fig. 7a). Spatially, this underestimation is most pronounced in regions of significant greening, such as southern China, the Loess Plateau, and northeastern China, while slight overestimation occurs in parts of northwestern China (Fig. 7a). At the river basin scale, the effect is strongest in the Pe. RB, with an average decrease of 71.15 mm yr^{-1}, and minimal in the In. RB, with a change of 1.96 mm yr^{-1} (Fig. 7c). In contrast, the impact of using radiation forcing is comparatively small, causing a marginal increase of 0.75% (2.93 mm yr^{-1}) in national mean ET. Spatially, the differences arising from default radiation estimates are primarily distributed over the eastern Tibetan Plateau and southern China (Fig. 7b). Across basins, the sensitivity to radiation is greatest in the Ye. RB, with an average effect of –7.15 mm yr^{-1}, and negligible in the SL RB at –0.05 mm yr^{-1} (Fig. 7d).

https://doi.org/10.5194/egusphere-2026-2505
Preprint. Discussion started: 29 June 2026

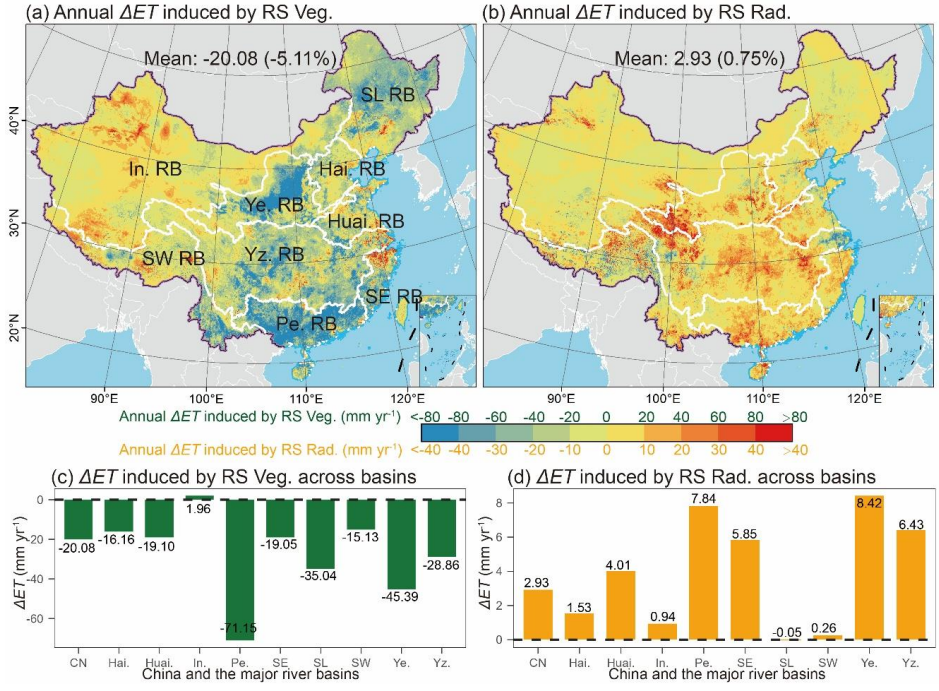

Fig. 7. Spatial distribution of ET simulated by the VIC model induced by (a) remote sensing vegetation dynamic data and (b) radiation dynamic data, and their differences (c, d) across river basins. Here, *ΔET* represents the difference between the simulation results of S2 and S1.

At the monthly scale, the impact of dynamic vegetation data on ET simulation intensifies from the period 2000–2005 to 2015–2020, with the difference being most pronounced during the vegetation growing season (May to October) (Fig. 8a). In contrast, the influence of dynamic radiation data shows minimal change in magnitude between these two periods, although its peak monthly effect shifts later by approximately one month (Fig. 8b). Seasonally, dynamic vegetation data has the strongest effect on ET in summer, with an average change of –7.91 mm season^{-1} (Fig. 8c). This seasonal variation is greatest in the Pe. RB and smallest in the In. RB. The impact of dynamic radiation data is more discernible in spring (1.09 mm season^{-1}) and summer (0.97 mm season^{-1}), with the most pronounced seasonal differences occurring in the Pe. RB and the Ye. RB (Fig. 8d).

https://doi.org/10.5194/egusphere-2026-2505
Preprint. Discussion started: 29 June 2026

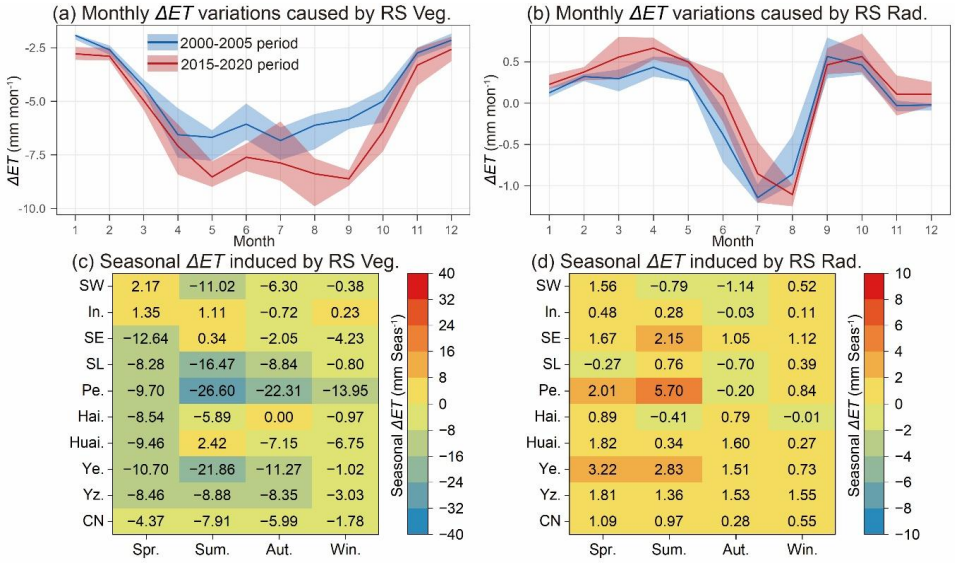

Fig. 8. Impacts of dynamic vegetation data and dynamic radiation data on ET simulation (a, b) at the monthly scale across different periods, and (c, d) at the seasonal scale for China and the nine major river basins. In panels a and b, the upper and lower bounds of the shaded area represent the 75th and 25th percentiles, respectively.

3.4. Impact of remote sensing data on model-simulated runoff

Regarding runoff simulation, disregarding vegetation dynamic data leads to a national mean overestimation of 14.13% (29.06 mm yr^{-1}) (Fig. 9a). Spatially, this overestimation is widespread across northwestern, northeastern, and southern China. Across different river basins, dynamic vegetation data has the greatest impact on runoff simulation in the Pe. RB, with an average increase of 68.87 mm yr^{-1}, and the smallest impact in the Huai. RB, with an average of 13.20 mm yr^{-1} (Fig. 9c). In contrast, omitting dynamic radiation data leads to a slight national mean underestimation of 1.95% (4.01 mm yr^{-1}). Spatially, the underestimated runoff is mainly distributed in the source regions of the Yangtze and Yellow Rivers in the eastern Tibetan Plateau (Fig. 9b). Across different river basins, dynamic radiation data has the greatest impact on runoff simulation in the SW RB, with an average effect of –11.30 mm yr^{-1}, and the smallest impact in the SL RB, with an average

https://doi.org/10.5194/egusphere-2026-2505
Preprint. Discussion started: 29 June 2026

effect of 0.31 mm yr⁻¹ (Fig. 9d).

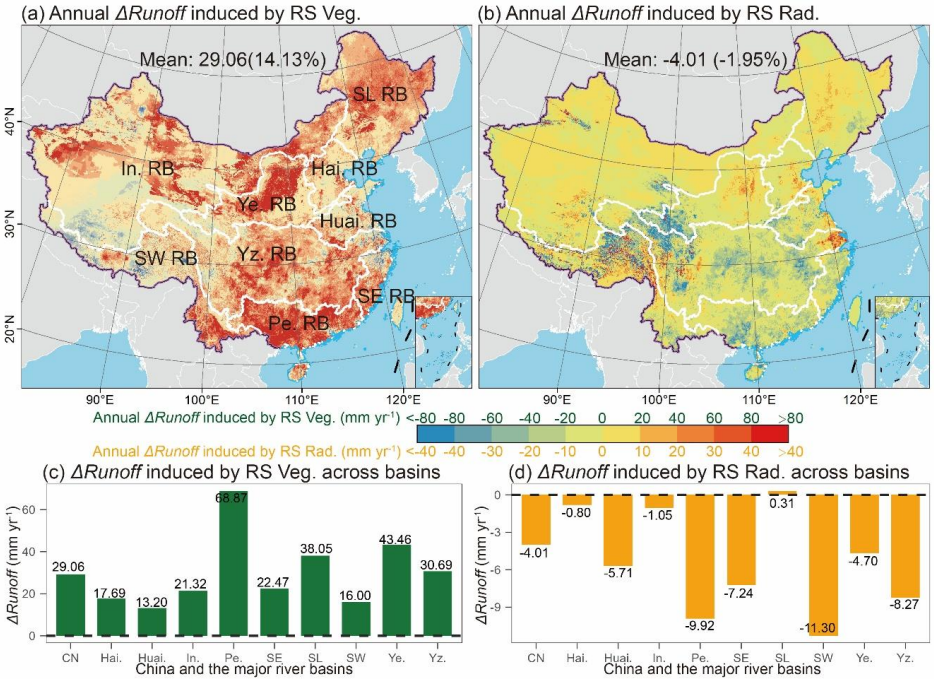

Fig. 9. Spatial distribution of runoff simulated by the VIC model induced by (a) remote sensing vegetation dynamic data and (b) radiation dynamic data, and their differences (c, d) across river basins. Here, *ΔRunoff* represents the difference between the simulation results of S3 and S1.

At the monthly scale, the influence of dynamic vegetation data on runoff strengthens from the period 2000–2005 to 2015–2020, with its peak shifting from July to August (Fig. 10a). Regarding the influence of dynamic radiation data on runoff simulation (Fig. 10b), the period 2015–2020 exhibits a stronger negative impact compared to 2000–2005, primarily occurring in June and July. Across different seasons, dynamic vegetation data exerts the greatest influence on runoff simulation in summer (9.57 mm seas⁻¹) (Fig. 10d). Among the river basins, the impact of dynamic vegetation data on runoff simulation is largest in the Pe. RB and smallest in the SW RB. The influence of dynamic radiation data on runoff is more apparent in summer (–1.90 mm seas⁻¹) and autumn (–0.94 mm seas⁻¹). Among the basins, seasonal differences in runoff induced by

https://doi.org/10.5194/egusphere-2026-2505
Preprint. Discussion started: 29 June 2026

dynamic radiation data are most prominent in the Southwest Rivers Basin (Fig. 10e).

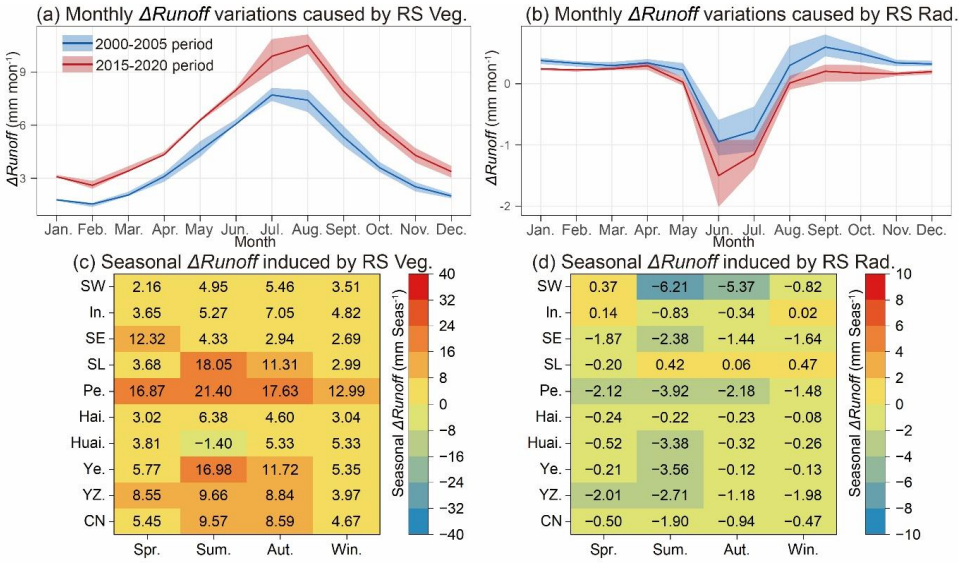

Fig. 10. Impacts of dynamic vegetation data and dynamic radiation data on runoff simulation (a, b) at the monthly scale across different periods, and (c, d) at the seasonal scale for China and the nine major river basins.

4. Discussion

4.1. Model reliability assessment

Evaluating runoff and ET performance across multiple scales is critical for assessing model reliability. Our results demonstrate that incorporating dynamic vegetation and radiation parameters into the VIC model yields favorable accuracy in simulating both runoff and ET (Figs. 3, 5, and 6). This improvement occurs because inputting dynamic parameters allows the model to capture the true interannual and seasonal fluctuations of vegetation and radiation states. Consequently, the VIC model can more accurately simulate key variables in land surface water and heat flux calculations that are altered by vegetation and radiation changes. Examples include canopy interception capacity and transpiration capacity modified by vegetation changes, and the total

https://doi.org/10.5194/egusphere-2026-2505
Preprint. Discussion started: 29 June 2026

energy available at the surface altered by radiation changes (Peng et al. 2024). Evaporation process is particularly sensitive to both vegetation and radiation changes (Yang et al. 2023b). Our validation results show good accuracy at both site and national scales (Figs. 5 and 6). Therefore, by providing an accurate representation of these key variables, the inclusion of dynamic vegetation and radiation parameters ultimately enhances the VIC model's simulation accuracy for runoff and ET.

Although we thoroughly consider the impact of dynamic vegetation and radiation parameters on VIC simulation performance, several other factors significantly influencing land surface water and energy simulations are not included in this study. Especially, the VIC model configuration used here does not account for strong human disturbances such as agricultural irrigation, reservoir construction, or urban expansion. Neglecting these processes may degrade model performance in some regions (Dombrowski et al. 2024; Wang et al. 2024; Zhang et al. 2025). However, the dynamic vegetation parameters used in this study partially reflect the impacts of human activities, such as ecological restoration projects. Moreover, at regional or continental scale as large as China, the influence of human activities such as urban expansion on the simulated accuracy of runoff and ET is relatively minor (Li et al. 2022; Tang et al. 2024; Wang et al. 2021).

LSMs have been widely applied in hydrologic research, yet parameter transfer to ungauged basins remains a major challenge (Guo et al. 2020; Raoult et al. 2025; Sytsma et al. 2022). To address this, mainstream approaches include parameter regionalization, donor-basin transfer, and transfer across hydroclimatically similar regions, as well as deep-learning methods developed on these frameworks (Hu et al. 2024; Kratzert et al. 2019; Yang et al. 2023a). For example, Zhu et al. (2021) calibrated and validated VIC model parameters using observed data from 29 Chinese basins

https://doi.org/10.5194/egusphere-2026-2505
Preprint. Discussion started: 29 June 2026

and transferred parameters based on similar climate zones. However, these methods do not adequately incorporate vegetation dynamics. Our parameter transfer framework employs a straightforward multiple linear regression method (Eq. 8). It integrates climatic background, vegetation attributes, and radiation parameters as predictors, enabling the model to achieve reliable performance in ungauged basins (Fig. 4). When dynamic vegetation parameters and radiation forcings are not included, the model simulation results may show a comparable R value (Fig. 11a), but the NSE, KGE, and Bias are all lower than those achieved with the fully dynamic parameter set (Figs. 11b-d). Notably, dynamic vegetation parameters have a particularly significant influence on simulation accuracy. Our findings therefore emphasize that dynamic vegetation parameters must be prioritized as a key constraint in large-scale hydrological modeling.

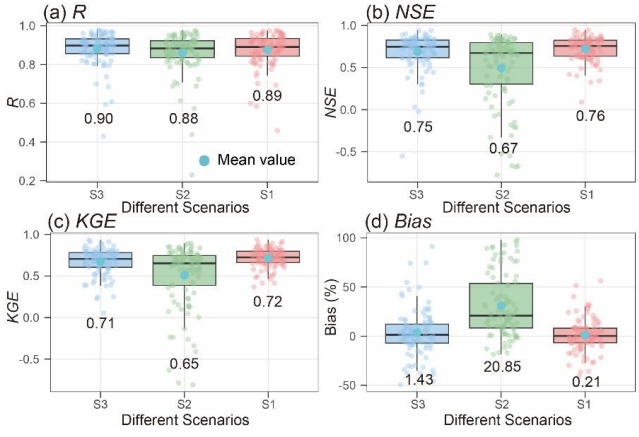

Fig. 11. Performance of the calibrated VIC model in simulating runoff under different scenarios. In the figure, S1 represents the scenario with all dynamic inputs, S2 the scenario with default/static vegetation data, and S3 the scenario with default radiation data.

4.2. Enhancing hydrological simulations with remote sensing parameters in LSMs

Since 2000, vegetation has experienced rapid greening driven by a series of ecological restoration programs across China (Chen et al. 2019; Jiang et al. 2022; Zhao et al. 2022). From the

https://doi.org/10.5194/egusphere-2026-2505
Preprint. Discussion started: 29 June 2026

perspective of LSM parameters, the most significant impacts of vegetation greening are on three key variables: LAI, FVC, and albedo, leading to significant increases in LAI and FVC and a decrease in albedo (Fig. 12a). These remote sensing vegetation parameters directly regulate key biophysical processes within LSMs, thereby exerting a fundamental control on the simulation of water and energy fluxes. Enhanced LAI and FVC, driven by widespread vegetation greening, increase canopy interception, transpiration, and surface albedo, which collectively alter the partitioning of available energy and water. Recent mechanistic studies corroborate this critical link. For example, Peng et al. (2024) demonstrated that integrating dynamic LAI and FVC into the VIC model significantly improved the accuracy of ET component partitioning. Similarly, He et al. (2024) showed that assimilating GLASS LAI and FVC into the Noah-MP model enhanced the simulation of land surface temperature. These findings collectively underscore that the dynamic representation of vegetation structure is not merely an input substitution but a critical step toward achieving physically consistent simulations of coupled water and heat fluxes in a changing environment. Our results also show that disregarding dynamic vegetation parameters causes the VIC model to underestimate ET by 5.11% and overestimate runoff by 14.13% on average. This effect is spatially concentrated in regions with significant vegetation greening, such as the Loess Plateau (Figs. 7a and 9a). As vegetation greening intensifies, its impact on ET during the growing season becomes greater (Fig. 8a), and the peak impact on runoff shifts later by one month (from July to August, Fig. 10a).

For the ET process, vegetation greening directly increases transpiration capacity and canopy interception capacity, thereby amplifying both Ec and T. Although this may suppress Es to some extent, the rapid growth in T and Ec collectively elevates total ET (Jiang et al. 2022; Peng et al.

https://doi.org/10.5194/egusphere-2026-2505
Preprint. Discussion started: 29 June 2026

2024). Since both T and Ec are closely linked to vegetation physiology, the influence of vegetation dynamics on ET during the growing season intensifies with the degree of greening. For runoff generation, vegetation greening reduces the amount of precipitation reaching the ground, making surface runoff generation more difficult, which delays the timing and peak intensity of runoff (Ficklin et al. 2024; Liu et al. 2025b; Yan et al. 2024b). Consequently, dynamic vegetation parameters not only control the spatial distribution of simulated hydrological fluxes but also influence their interannual and seasonal variation patterns. In the current context of frequent meteorological droughts and floods, accurately accounting for vegetation dynamics becomes even more critical for enhancing the simulation and forecasting accuracy of LSMs.

Regarding radiation changes, a significant decreasing trend in Rs and an increasing trend in Rl were observed in China from 2000 to 2020 (Fig. 12b). Radiation dynamics affect the direct energy source for ET and also influence runoff and ET by controlling the timing and intensity of snow and ice melt (Deng et al. 2025). Under the default radiation setting, the VIC model uses the MTCLIM and Prata algorithms to calculate daily Rs and Rl based on meteorological forcing data for each grid cell (Prata 1995; Running et al. 1987). However, this approach not only risks propagating errors introduced during the generation of meteorological forcing data (e.g., through spatial interpolation) but also causes substantial uncertainty in topographically complex regions (Hirata et al. 2020; Yin et al. 2026). River source regions, such as the southeastern Tibetan Plateau, often feature highly complex terrain and are critical zones for snow and ice melt (Deng et al. 2025; Li et al. 2025). This explains why our results show a greater impact of dynamic radiation parameters on ET and runoff in the southeastern Tibetan Plateau and the Tianshan region of northwestern China (Figs. 7b and 9b).

https://doi.org/10.5194/egusphere-2026-2505
Preprint. Discussion started: 29 June 2026

In summary, given the very significant overall vegetation changes across China—with LAI and FVC showing highly significant increasing trends and albedo a decreasing trend (Fig. 12a)—and the significant decreasing trend in Rs and increasing trend in Rl within the radiation components (Fig. 12b), changes in these variables exhibit strong correlations with ET and runoff simulations (Figs. 12c and d). Therefore, inputting accurate dynamic parameters into the model is essential for achieving precise simulations, with the role of dynamic vegetation parameters requiring particular attention.

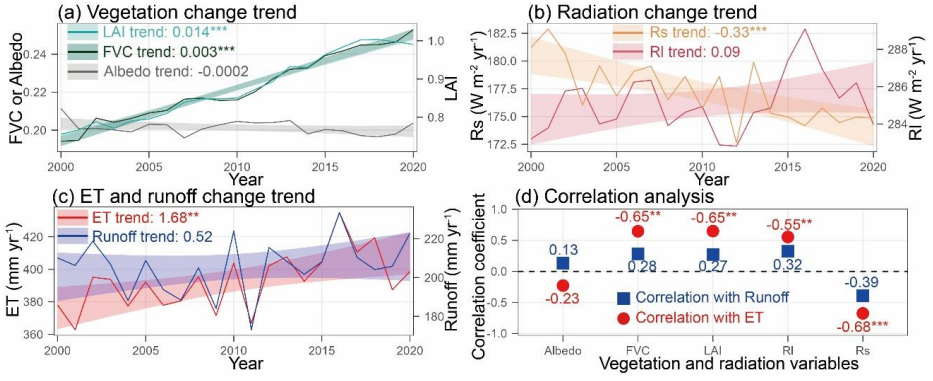

Fig. 12. Trends in (a) vegetation, (b) radiation, and (c) ET and Runoff across China from 2000 to 2020, and (d) correlations between various vegetation/radiation factors and ET/Runoff. In the figure, *** denotes $p < 0.001$, and ** denotes $p < 0.01$. In panels a-c, the colored band beneath the line represents the corresponding trend confidence interval.

4.3. Limitations and Future work

Although we incorporate dynamic vegetation and radiation parameters into the VIC model and conduct comprehensive calibration and validation of the model simulations, some uncertainties may still remain in our results. First, our simulations do not account for the effects of changing CO_2 concentration on vegetation physiology, which limits our analysis of the model performance for carbon-cycle simulations. Second, land use types in the model are not dynamic,

https://doi.org/10.5194/egusphere-2026-2505
Preprint. Discussion started: 29 June 2026

which may introduce uncertainty in simulated transpiration. However, for total ET at large spatial scales, the impact of LUCC is relatively small (Li et al. 2022), and the dynamic vegetation parameters we use can also partly reflect changes in vegetation types. Finally, our study does not explore the impacts of dynamic vegetation and radiation factors on other key hydrologic components, such as soil moisture and groundwater. This is because, compared with runoff and ET, these hydrologic variables show smaller changes, or reliable observations are difficult to obtain for evaluating simulation accuracy. This remains an important direction for future work.

For the remote sensing-based dynamic vegetation and radiation parameters, although the products we use are of good quality and have been widely adopted as forcing for land surface models, reliance on a single product may introduce uncertainty (Jiang et al. 2022; Peng et al. 2024). Such uncertainties, arising from both the retrieval process and spatiotemporal resampling, can propagate into the VIC simulations and bias the results. Our findings should therefore be interpreted as the model response under the selected remote sensing forcing, rather than as a unique estimate of the true land surface processes. Future work should compare multiple remote sensing products and use independent observations to further quantify how uncertainties in these inputs influence model outcomes.

With the rapid advancement of remote sensing data, an increasing number of model forcing variables can now be retrieved through inversion. Initially, using remote sensing data to replace intermediate variables calculated internally by models can significantly enhance simulation accuracy. For example, Liu et al. (2025a) incorporated soil moisture data as a model input to achieve precise ET estimation. Furthermore, the emergence of higher-resolution remote sensing data for land surface characteristics provides a foundation for LSM simulations at finer scales

https://doi.org/10.5194/egusphere-2026-2505
Preprint. Discussion started: 29 June 2026

(Shangguan et al. 2013; Shi et al. 2025; Yang and Huang 2021; Zhang et al. 2021). Moreover, the development of novel vegetation dynamic datasets, such as tree height, and tree age, holds promise for offering greater benefits to LSM simulation and development in the future (Hunter et al. 2025; Lin et al. 2023). Therefore, we argue that employing high-accuracy remote sensing data to replace the estimation of certain variables is an effective strategy for reducing uncertainties inherent in different LSMs during simulation and for achieving higher model simulation accuracy.

5. Conclusion

This study investigates the differential effects of various remote sensing dynamic parameters on the simulation of hydrological cycle variables by incorporating remote sensing vegetation and radiation dynamic data into the land surface model VIC. We not only calibrate and validate model parameters using multiple runoff and ET from in-situ observations and remote sensing products, but also elucidate the mechanism through which remote sensing dynamic data influence hydrological simulations from the perspective of model physics. This approach addresses uncertainties introduced by traditional modeling due to static model parameters, providing effective support for the development of coupled LSMs and remote sensing data applications.

After incorporating dynamic vegetation and radiation data into the VIC model, we conduct comprehensive calibration and validation using runoff monitoring data from 41 sub-basins within China. During the validation period, the model achieves average performance metrics of R=0.86, NSE=0.68, KGE=0.71, and Bias=–0.08%. For ungauged basins, parameters are transferred using a multiple linear regression model. Validation results show clear improvements across all metrics compared to those obtained with default parameters. Regarding ET simulation, comparisons with site observations and multiple existing ET products confirm the high accuracy of the model

https://doi.org/10.5194/egusphere-2026-2505
Preprint. Discussion started: 29 June 2026

simulations. Incorporating dynamic vegetation forcing reduces the bias associated with static vegetation inputs, avoiding a 5.11% (20.08 mm yr^{-1}) underestimation of ET and a 14.13% (29.06 mm yr^{-1}) overestimation of runoff. This effect is more pronounced in areas with significant vegetation greening. Dynamic radiation data has a smaller impact on the simulation results, exerting a greater influence primarily in the eastern Tibetan Plateau.

Our findings indicate that dynamic vegetation data has a significant impact on land surface model simulations and requires prioritized consideration. The influence of remote sensing radiation dynamic data is more prominent in localized, topographically complex regions. By investigating the effects of remote sensing parameters on key components of the water cycle in land surface models, this study reveals the mechanisms through which dynamic vegetation and radiation influence LSMs simulations, with particular emphasis on the importance of vegetation dynamics. These results provide a valuable reference for optimizing land surface model parameterization schemes and enhancing the accuracy of high-precision digital Earth simulations.

Acknowledgment

This study was supported by a grant from the National Natural Science Foundation of China (No. 42271021).

References:

Alkama, R., Forzieri, G., Duveiller, G., Grassi, G., Liang, S., & Cescatti, A. (2022). Vegetation-based climate mitigation in a warmer and greener World. *Nature Communications, 13* (1). https://doi.org/10.1038/s41467-022-28305-9.

Arsenault, K.R., Nearing, G.S., Wang, S., Yatheendradas, S., & Peters-Lidard, C.D.J.J.o.H. (2018). Parameter sensitivity of the Noah-MP land surface model with dynamic vegetation, *19* (5), 815-830.

Bohn, T.J., Podest, E., Schroeder, R., Pinto, N., McDonald, K.C., Glagolev, M., Filippov, I., Maksyutov, S., Heimann, M., Chen, X., & Lettenmaier, D.P. (2013). Modeling the large-scale effects of surface moisture heterogeneity on wetland carbon fluxes in the West Siberian Lowland. *Biogeosciences, 10* (10), 6559-6576.

https://doi.org/10.5194/egusphere-2026-2505
Preprint. Discussion started: 29 June 2026

https://doi.org/10.5194/bg-10-6559-2013.
Bohn, T.J., & Vivoni, E.R. (2016). Process-based characterization of evapotranspiration sources over the North American monsoon region. *Water Resour. Res., 52* (1), 358-384. https://doi.org/10.1002/2015wr017934.
Bonan, G.B., & Levis, S. (2006). Evaluating aspects of the community land and atmosphere models (CLM3 and CAM3) using a dynamic global vegetation model. *Journal of Climate*
19 (11), 2290-2301.
Bonan, G.B., Oleson, K.W., Vertenstein, M., Levis, S., Zeng, X., Dai, Y., Dickinson, R.E., & Yang, Z.-L. (2002). The land surface climatology of the Community Land Model coupled to the NCAR Community Climate Model. *J. Climate, 15* (22), 3123-3149.
Brekke, L.D., Pruitt, T., Gangopadhyay, S., Elsner, M.M., Mizukami, N., & Clark, M.P. (2014). How Does the Choice of Distributed Meteorological Data Affect Hydrologic Model Calibration and Streamflow Simulations? *J. Hydrometeorol., 15* (4), 1384-1403. https://doi.org/10.1175/jhm-d-13-083.1.
Cao, S., Li, M., Zhu, Z., Wang, Z., Zha, J., Zhao, W., Duanmu, Z., Chen, J., Zheng, Y., Chen, Y., Myneni, R.B., & Piao, S. (2023). Spatiotemporally consistent global dataset of the GIMMS leaf area index (GIMMS LAI4g) from 1982 to 2020. *Earth System Science Data, 15* (11), 4877-4899. https://doi.org/10.5194/essd-15-4877-2023.
Chen, C., Park, T., Wang, X., Piao, S., Xu, B., Chaturvedi, R.K., Fuchs, R., Brovkin, V., Ciais, P., Fensholt, R., Tømmervik, H., Bala, G., Zhu, Z., Nemani, R.R., & Myneni, R.B. (2019). China and India lead in greening of the world through land-use management. *Nat. Sustain., 2* (2), 122-129. https://doi.org/10.1038/s41893-019-0220-7.
Cheng, J., & Liang, S. (2016). Global Estimates for High-Spatial-Resolution Clear-Sky Land Surface Upwelling Longwave Radiation From MODIS Data. *IEEE Trans. Geosci. Remote Sens., 54* (7), 4115-4129. https://doi.org/10.1109/tgrs.2016.2537650.
de Ávila, Á.V.A., de Gonçalves, L.G.G., Souza, V.d.A., Alves, L.E.R., Galetti, G.D., Maske, B.M., Getirana, A., Ruhoff, A., Biudes, M.S., Machado, N.G., & Roberti, D.R. (2023). Assessing the Performance of the South American Land Data Assimilation System Version 2 (SALDAS-2) Energy Balance across Diverse Biomes. *Atmosphere, 14* (6). https://doi.org/10.3390/atmos14060959.
Deng, G., Zhang, T., Liu, X., He, Y., Chen, H., Shen, Q., Chen, Q., & Tang, Z. (2025). Intensifying heatwave events affect snow phenology over the Tibetan Plateau. *J. Hydrol, 659*. https://doi.org/10.1016/j.jhydrol.2025.133293.
Dickinson, R.E.J.T.r., National Center for Research. (1986). Biosphere/atmosphere transfer scheme (BATS) for the NCAR community climate model.
Dombrowski, O., Brogi, C., Hendricks Franssen, H.J., Pisinaras, V., Panagopoulos, A., Swenson, S., & Bogena, H. (2024). Land Surface Modeling as a Tool to Explore Sustainable Irrigation Practices in Mediterranean Fruit Orchards. *Water Resour. Res., 60* (7). https://doi.org/10.1029/2023wr036139.
Dong, W., Yuan, H., Lin, W., Liu, Z., Xiang, J., Wei, Z., Li, L., Li, Q., & Dai, Y. (2025). A global urban tree leaf area index dataset for urban climate modeling. *Sci. Data, 12* (1). https://doi.org/10.1038/s41597-025-04729-y.
Duveiller, G., Hooker, J., & Cescatti, A. (2018). The mark of vegetation change on Earth's surface energy balance. *Nature Communications, 9* (1). https://doi.org/10.1038/s41467-017-02810-8.
Ficklin, D.L., Touma, D., Cook, B.I., Robeson, S.M., Hwang, T., Scheff, J., Williams, A.P., Watson, H., Livneh, B., Tye, M.R., & Wang, L. (2024). Vegetation Greening Mitigates the Impacts of Increasing Extreme Rainfall on Runoff Events. *Earth's Future, 12* (12). https://doi.org/10.1029/2024ef004661.
Findell, K.L., Berg, A., Gentine, P., Krasting, J.P., Lintner, B.R., Malyshev, S., Santanello, J.A., & Shevliakova, E. (2017). The impact of anthropogenic land use and land cover change on regional climate extremes. *Nature Communications, 8* (1). https://doi.org/10.1038/s41467-017-01038-w.
Guo, Y., Cheng, J., & Liang, S. (2018). Comprehensive assessment of parameterization methods for estimating

https://doi.org/10.5194/egusphere-2026-2505
Preprint. Discussion started: 29 June 2026

clear-sky surface downward longwave radiation. *Theoretical and Applied Climatology, 135* (3-4), 1045-1058. https://doi.org/10.1007/s00704-018-2423-7.

Guo, Y., Zhang, Y., Zhang, L., & Wang, Z. (2020). Regionalization of hydrological modeling for predicting streamflow in ungauged catchments: A comprehensive review. *WIREs Water, 8* (1). https://doi.org/10.1002/wat2.1487.

He, J., Yang, K., Tang, W., Lu, H., Qin, J., Chen, Y., & Li, X. (2020). The first high-resolution meteorological forcing dataset for land process studies over China. *Sci. Data, 7* (1). https://doi.org/10.1038/s41597-020-0369-y.

Hirata, A., Kominami, Y., Matsui, T., & Hijioka, Y. (2020). Evaluation of the estimation of shortwave solar radiation in Japan using the Mountain Microclimate Simulation Model. *Journal of Agricultural Meteorology, 76* (2), 96-103. https://doi.org/10.2480/agrmet.D-19-00046.

Hu, C., Xia, J., She, D., Jing, Z., Hong, S., Song, Z., & Wang, G. (2024). Parameter Regionalization With Donor Catchment Clustering Improves Urban Flood Modeling in Ungauged Urban Catchments. *Water Resour. Res., 60* (7). https://doi.org/10.1029/2023wr035071.

Hunter, M.O., Parente, L., Ho, Y.-f., Bonannella, C., Guimarães Ferreira, L., Morton, D., Consoli, D., & Sloat, L. (2025). Global 30-m annual median vegetation height maps (2000–2022) based on ICESat-2 data and Machine Learning. *Sci. Data, 12* (1). https://doi.org/10.1038/s41597-025-05739-6.

Huo, X., Fox, A.M., Dashti, H., Devine, C., Gallery, W., Smith, W.K., Raczka, B., Anderson, J.L., Rogers, A., & Moore, D.J.P. (2024). Integrating State Data Assimilation and Innovative Model Parameterization Reduces Simulated Carbon Uptake in the Arctic and Boreal Region. *J. Geophys Res.- Biogeo., 129* (9). https://doi.org/10.1029/2024jg008004.

Jia, K., Liang, S., Gu, X., Baret, F., Wei, X., Wang, X., Yao, Y., Yang, L., & Li, Y. (2016). Fractional vegetation cover estimation algorithm for Chinese GF-1 wide field view data. *Remote Sens. Environ., 177*, 184-191. https://doi.org/https://doi.org/10.1016/j.rse.2016.02.019.

Jiang, F., Xie, X., Wang, Y., Liang, S., Zhu, B., Meng, S., Zhang, X., Chen, Y., & Liu, Y. (2022). Vegetation greening intensified transpiration but constrained soil evaporation on the Loess Plateau. *J. Hydrol, 614*, 128514. https://doi.org/10.1016/j.jhydrol.2022.128514.

Kratzert, F., Klotz, D., Herrnegger, M., Sampson, A.K., Hochreiter, S., & Nearing, G.S. (2019). Toward Improved Predictions in Ungauged Basins: Exploiting the Power of Machine Learning. *Water Resour. Res., 55* (12), 11344-11354. https://doi.org/10.1029/2019wr026065.

Lawrence, D.M., Fisher, R.A., Koven, C.D., Oleson, K.W., Swenson, S.C., Bonan, G., Collier, N., Ghimire, B., van Kampenhout, L., Kennedy, D., Kluzek, E., Lawrence, P.J., Li, F., Li, H., Lombardozzi, D., Riley, W.J., Sacks, W.J., Shi, M., Vertenstein, M., Wieder, W.R., Xu, C., Ali, A.A., Badger, A.M., Bisht, G., van den Broeke, M., Brunke, M.A., Burns, S.P., Buzan, J., Clark, M., Craig, A., Dahlin, K., Drewniak, B., Fisher, J.B., Flanner, M., Fox, A.M., Gentine, P., Hoffman, F., Keppel-Aleks, G., Knox, R., Kumar, S., Lenaerts, J., Leung, L.R., Lipscomb, W.H., Lu, Y., Pandey, A., Pelletier, J.D., Perket, J., Randerson, J.T., Ricciuto, D.M., Sanderson, B.M., Slater, A., Subin, Z.M., Tang, J., Thomas, R.Q., Val Martin, M., & Zeng, X. (2019). The Community Land Model Version 5: Description of New Features, Benchmarking, and Impact of Forcing Uncertainty. *J. Adv. Model. Earth Sy., 11* (12), 4245-4287. https://doi.org/10.1029/2018ms001583.

Li, X., Zou, L., Xia, J., Dou, M., Li, H., & Song, Z. (2022). Untangling the effects of climate change and land use/cover change on spatiotemporal variation of evapotranspiration over China. *J. Hydrol, 612*. https://doi.org/10.1016/j.jhydrol.2022.128189.

Li, Z., Guo, W., Wang, Y., Zhang, Y., Zhang, S., Zhu, X., & Xu, N. (2025). Glacier melting phenology changes in the Tibetan Plateau from 1981 to 2020. *Catena, 257*. https://doi.org/10.1016/j.catena.2025.109199.

Liang, S., Cheng, J., Jia, K., Jiang, B., Liu, Q., Xiao, Z., Yao, Y., Yuan, W., Zhang, X., Zhao, X., & Zhou, J. (2021).

https://doi.org/10.5194/egusphere-2026-2505
Preprint. Discussion started: 29 June 2026

The Global Land Surface Satellite (GLASS) Product Suite. *Bull. Am. Meteorol. Soc., 102* (2), E323-E337. https://doi.org/10.1175/bams-d-18-0341.1.

Liang, S., Zhao, X., Liu, S., Yuan, W., Cheng, X., Xiao, Z., Zhang, X., Liu, Q., Cheng, J., Tang, H., Qu, Y., Bo, Y., Qu, Y., Ren, H., Yu, K., & Townshend, J. (2013). A long-term Global LAnd Surface Satellite (GLASS) data-set for environmental studies. *International Journal of Digital Earth, 6* (sup1), 5-33. https://doi.org/10.1080/17538947.2013.805262.

Liang, X., Lettenmaier, D.P., Wood, E.F., & Burges, S.J. (1994). A simple hydrologically based model of land surface water and energy fluxes for general circulation models. *J. Geophys Res.-Atmos., 99* (D7), 14415-14428. https://doi.org/10.1029/94JD00483.

Lin, X., Shang, R., Chen, J.M., Zhao, G., Zhang, X., Huang, Y., Yu, G., He, N., Xu, L., & Jiao, W. (2023). High-resolution forest age mapping based on forest height maps derived from GEDI and ICESat-2 space-borne lidar data. *Agric. For. Meteorol, 339*. https://doi.org/10.1016/j.agrformet.2023.109592.

Liu, M., Lin, K., & Tu, X. (2025a). Increasing Evapotranspiration in China: Quantifying the Roles of CO2 Fertilization, Climate and Vegetation Changes. *Water Resour. Res., 61* (2). https://doi.org/10.1029/2024wr038148.

Liu, Q., Wang, L., Qu, Y., Liu, N., Liu, S., Tang, H., & Liang, S. (2013). Preliminary evaluation of the long-term GLASS albedo product. *International Journal of Digital Earth, 6* (sup1), 69-95. https://doi.org/10.1080/17538947.2013.804601.

Liu, S., Seybold, H., van Meerveld, I., Wang, Y., & Kirchner, J.W. (2025b). Tree planting and soil conservation measures have strongly attenuated storm runoff responses on the Chinese Loess Plateau. *J. Hydrol, 662*. https://doi.org/10.1016/j.jhydrol.2025.134039.

Lombardozzi, D.L., Bonan, G.B., Smith, N.G., Dukes, J.S., & Fisher, R.A. (2015). Temperature acclimation of photosynthesis and respiration: A key uncertainty in the carbon cycle-climate feedback. *Geophys. Res. Lett., 42* (20), 8624-8631. https://doi.org/10.1002/2015gl065934.

Manabe, S.J.M.w.r. (1969). Climate and the ocean circulation: I. The atmospheric circulation and the hydrology of the earth's surface*, 97* (11), 739-774.

Meng, S., Xie, X., Zhu, B., & Wang, Y. (2020). The relative contribution of vegetation greening to the hydrological cycle in the Three-North region of China: A modelling analysis. *J. Hydrol, 591*, 125689. https://doi.org/10.1016/j.jhydrol.2020.125689.

Miralles, D.G., Bonte, O., Koppa, A., Baez-Villanueva, O.M., Tronquo, E., Zhong, F., Beck, H.E., Hulsman, P., Dorigo, W., Verhoest, N.E.C., & Haghdoost, S. (2025). GLEAM4: global land evaporation and soil moisture dataset at 0.1° resolution from 1980 to near present. *Sci. Data, 12* (1). https://doi.org/10.1038/s41597-025-04610-y.

Nijssen, B., Schnur, R., & Lettenmaier, D.P. (2001). Global Retrospective Estimation of Soil Moisture Using the Variable Infiltration Capacity Land Surface Model, 1980–93. *J. Climate, 14* (8), 1790-1808. https://doi.org/https://doi.org/10.1175/1520-0442(2001)014<1790:GREOSM>2.0.CO;2.

Niu, G.-Y., Yang, Z.-L., Mitchell, K.E., Chen, F., Ek, M.B., Barlage, M., Kumar, A., Manning, K., Niyogi, D., Rosero, E., Tewari, M., & Xia, Y. (2011). The community Noah land surface model with multiparameterization options (Noah-MP): 1. Model description and evaluation with local-scale measurements. *Journal of Geophysical Research, 116* (D12). https://doi.org/10.1029/2010jd015139.

Peng, D., Xie, X., Liang, S., Wang, Y., Tursun, A., Liu, Y., Jia, K., Ma, H., & Chen, Y. (2024). Improving evapotranspiration partitioning by integrating satellite vegetation parameters into a land surface model. *J. Hydrol, 643*. https://doi.org/10.1016/j.jhydrol.2024.131928.

Piao, S., Wang, X., Park, T., Chen, C., Lian, X., He, Y., Bjerke, J.W., Chen, A., Ciais, P., Tømmervik, H., Nemani, R.R.,

https://doi.org/10.5194/egusphere-2026-2505
Preprint. Discussion started: 29 June 2026

& Myneni, R.B. (2020). Characteristics, drivers and feedbacks of global greening. *Nat. Rev. Earth Env., 1* (1), 14-27. https://doi.org/10.1038/s43017-019-0001-x.

Pitman, A.J. (2003). The evolution of, and revolution in, land surface schemes designed for climate models. *Int. J. Climatol., 23* (5), 479-510. https://doi.org/10.1002/joc.893.

Prata, A.J. (1995). A new long-wave formula for estimating downward clear-sky radiation at the surface. *Q. J. Roy. Meteor. Soc., 122* (533), 1127-1151. https://doi.org/10.1002/qj.49712253306.

Rajão, P.H.M., Berg, M.P., Cornelissen, J.H.C., & Dias, A.T.C. (2023). The effects of leaf traits on litter rainfall interception with consequences for runoff and soil conservation. *Journal of Ecology, 111* (12), 2662-2675. https://doi.org/10.1111/1365-2745.14203.

Raoult, N., Douglas, N., MacBean, N., Kolassa, J., Quaife, T., Roberts, A.G., Fisher, R., Fer, I., Bacour, C., Dagon, K., Hawkins, L., Carvalhais, N., Cooper, E., Dietze, M.C., Gentine, P., Kaminski, T., Kennedy, D., Liddy, H.M., Moore, D.J.P., Peylin, P., Pinnington, E., Sanderson, B., Scholze, M., Seiler, C., Smallman, T.L., Vergopolan, N., Viskari, T., Williams, M., & Zobitz, J. (2025). Parameter Estimation in Land Surface Models: Challenges and Opportunities With Data Assimilation and Machine Learning. *J. Adv. Model. Earth Sy., 17* (11). https://doi.org/10.1029/2024ms004733.

Running, S.W., Nemani, R.R., & Hungerford, R.D. (1987). Extrapolation of synoptic meteorological data in mountainous terrain and its use for simulating forest evapotranspiration and photosynthesis. *Canadian Journal of Forest Research, 17* (6), 472-483. https://doi.org/10.1139/x87-081.

Sato, H., Ito, A., Ito, A., Ise, T., & Kato, E. (2014). Current status and future of land surface models. *Soil Sci. Plant Nutr., 61* (1), 34-47. https://doi.org/10.1080/00380768.2014.917593.

Sellers, P.J., Mintz, Y., Sud, Y.C., & Dalcher, A. (1986). A Simple Biosphere Model (SIB) for Use within General Circulation Models %J Journal of Atmospheric Sciences, *43* (6), 505-531. https://doi.org/https://doi.org/10.1175/1520-0469(1986)043<0505:ASBMFU>2.0.CO;2.

Shangguan, W., Dai, Y., Liu, B., Zhu, A., Duan, Q., Wu, L., Ji, D., Ye, A., Yuan, H., Zhang, Q., Chen, D., Chen, M., Chu, J., Dou, Y., Guo, J., Li, H., Li, J., Liang, L., Liang, X., Liu, H., Liu, S., Miao, C., & Zhang, Y. (2013). A China data set of soil properties for land surface modeling. *J. Adv. Model. Earth Sy., 5* (2), 212-224. https://doi.org/10.1002/jame.20026.

Shi, G., Sun, W., Shangguan, W., Wei, Z., Yuan, H., Li, L., Sun, X., Zhang, Y., Liang, H., Li, D., Huang, F., Li, Q., & Dai, Y. (2025). A China dataset of soil properties for land surface modelling (version 2, CSDLv2). *Earth System Science Data, 17* (2), 517-543. https://doi.org/10.5194/essd-17-517-2025.

Shi, P., Lu, H., Leung, L.R., He, Y., Wang, B., Yang, K., Yu, L., Liu, L., Huang, W., Xu, S., Liu, J., Huang, X., Li, L., & Lin, Y. (2021). Significant Land Contributions to Interannual Predictability of East Asian Summer Monsoon Rainfall. *Earth's Future, 9* (2). https://doi.org/10.1029/2020ef001762.

Shrestha, R.R., Cannon, A.J., Hoffman, S., Whibley, M., & Lima, A. (2025). Benchmarking historical performance and future projections from a large-scale hydrologic model with a watershed hydrologic model. *Hydrol. Earth Syst. Sci., 29* (13), 2881-2900. https://doi.org/10.5194/hess-29-2881-2025.

Silwimba, K., Flores, A.N., Cionni, I., Billings, S.A., Sullivan, P.L., Ajami, H., Hirmas, D.R., & Li, L. (2025). Soil parameterization in land surface models drives large discrepancies in soil moisture predictions across hydrologically complex regions of the contiguous United States. *Geosci. Model Dev., 18* (20), 7707-7734. https://doi.org/10.5194/gmd-18-7707-2025.

Singh, V.P. (2018). Hydrologic modeling: progress and future directions. *Geoscience Letters, 5* (1). https://doi.org/10.1186/s40562-018-0113-z.

Sytsma, A., Crompton, O., Panos, C., Thompson, S., & Mathias Kondolf, G. (2022). Quantifying the Uncertainty Created by Non-Transferable Model Calibrations Across Climate and Land Cover Scenarios: A Case Study With

https://doi.org/10.5194/egusphere-2026-2505
Preprint. Discussion started: 29 June 2026

SWMM. *Water Resour. Res., 58* (2). https://doi.org/10.1029/2021wr031603.
Tang, Z., Ba, H., Zhang, W., & Zhang, Y. (2025). Dual function of root systems in balancing soil water flow behavior. *Communications Earth & Environment, 7* (1). https://doi.org/10.1038/s43247-025-03062-x.
Tang, Z., Wang, P., Li, Y., Sheng, Y., Wang, B., Popovych, N., & Hu, T. (2024). Contributions of climate change and urbanization to urban flood hazard changes in China's 293 major cities since 1980. *Journal of Environmental Management, 353*. https://doi.org/10.1016/j.jenvman.2024.120113.
Wang, Q., Cheng, L., Zhang, L., Liu, P., Qin, S., Liu, L., & Jing, Z. (2021). Quantifying the impacts of land-cover changes on global evapotranspiration based on the continuous remote sensing observations during 1982–2016. *J. Hydrol, 598*. https://doi.org/10.1016/j.jhydrol.2021.126231.
Wang, Y., Xie, X., Zhu, B., Tursun, A., Jiang, F., Liu, Y., Peng, D., & Zheng, B. (2024). An urban module coupled with the Variable Infiltration Capacity model to improve hydrothermal simulations in urban systems. *Geosci. Model Dev., 17* (15), 5803-5819. https://doi.org/10.5194/gmd-17-5803-2024.
Xiao, Z., Liang, S., Wang, J., Chen, P., Yin, X., Zhang, L., & Song, J. (2014). Use of General Regression Neural Networks for Generating the GLASS Leaf Area Index Product From Time-Series MODIS Surface Reflectance. *IEEE Trans. Geosci. Remote Sens., 52* (1), 209-223. https://doi.org/10.1109/tgrs.2013.2237780.
Xie, X., Liang, S., Yao, Y., Jia, K., Meng, S., & Li, J. (2015). Detection and attribution of changes in hydrological cycle over the Three-North region of China: Climate change versus afforestation effect. *Agric. For. Meteorol, 203*, 74-87. https://doi.org/10.1016/j.agrformet.2015.01.003.
Yan, K., Wang, J., Peng, R., Yang, K., Chen, X., Yin, G., Dong, J., Weiss, M., Pu, J., & Myneni, R.B. (2024a). HiQ-LAI: a high-quality reprocessed MODIS leaf area index dataset with better spatiotemporal consistency from 2000 to 2022. *Earth System Science Data, 16* (3), 1601-1622. https://doi.org/10.5194/essd-16-1601-2024.
Yan, X., Nunes, J.P., Sun, J., Tang, D.W.S., Wen, Y., & Li, Z. (2024b). Restored vegetation dominates the decrease in surface and subsurface runoff on the Loess Plateau. *J. Hydrol, 640*. https://doi.org/10.1016/j.jhydrol.2024.131730.
Yan, Y., Tang, J., Wang, S., Niu, X., & Le, W. (2021). Uncertainty of land surface model and land use data on WRF model simulations over China. *Climate Dynamics, 57* (7-8), 1833-1851. https://doi.org/10.1007/s00382-021-05778-w.
Yang, J., & Huang, X. (2021). The 30 m annual land cover dataset and its dynamics in China from 1990 to 2019. *Earth System Science Data, 13* (8), 3907-3925. https://doi.org/10.5194/essd-13-3907-2021.
Yang, X., Li, F., Qi, W., Zhang, M., Yu, C., & Xu, C.-Y. (2023a). Regionalization methods for PUB: a comprehensive review of progress after the PUB decade. *Hydrology Research, 54* (7), 885-900. https://doi.org/10.2166/nh.2023.027.
Yang, Y., Roderick, M.L., Guo, H., Miralles, D.G., Zhang, L., Fatichi, S., Luo, X., Zhang, Y., McVicar, T.R., Tu, Z., Keenan, T.F., Fisher, J.B., Gan, R., Zhang, X., Piao, S., Zhang, B., & Yang, D. (2023b). Evapotranspiration on a greening Earth. *Nat. Rev. Earth Env., 4* (9), 626-641. https://doi.org/10.1038/s43017-023-00464-3.
Yao, Y., Liang, S., Li, X., Chen, J., Wang, K., Jia, K., Cheng, J., Jiang, B., Fisher, J.B., Mu, Q., Grünwald, T., Bernhofer, C., & Roupsard, O. (2015). A satellite-based hybrid algorithm to determine the Priestley–Taylor parameter for global terrestrial latent heat flux estimation across multiple biomes. *Remote Sens. Environ., 165*, 216-233. https://doi.org/10.1016/j.rse.2015.05.013.
Yao, Y., Liang, S., Li, X., Hong, Y., Fisher, J.B., Zhang, N., Chen, J., Cheng, J., Zhao, S., Zhang, X., Jiang, B., Sun, L., Jia, K., Wang, K., Chen, Y., Mu, Q., & Feng, F. (2014). Bayesian multimodel estimation of global terrestrial latent heat flux from eddy covariance, meteorological, and satellite observations. *J. Geophys Res.-Atmos., 119* (8), 4521-4545. https://doi.org/10.1002/2013jd020864.
Yin, K., Zhang, X., Xie, J., Yang, H., Tan, J., Lin, F., & Liu, J. (2026). Modeling of longwave radiation on coastal

https://doi.org/10.5194/egusphere-2026-2505
Preprint. Discussion started: 29 June 2026

building façades based on field measurements. *Building and Environment, 287*. https://doi.org/10.1016/j.buildenv.2025.113859.

Zhang, L., Li, L., Zhang, Z., Arnault, J., Sobolowski, S., Chen, X., Lu, J., Mwanthi, A.M., Kad, P., Hassan, M.A., Portele, T., Kunstmann, H., & Zuo, Z. (2025). Enhanced hydrological modeling with the WRF-Hydro lake–reservoir module at a convection-permitting scale: a case study of the Tana River basin in East Africa. *Hydrol. Earth Syst. Sci., 29* (17), 4109-4132. https://doi.org/10.5194/hess-29-4109-2025.

Zhang, X., Liang, S., Zhou, G., Wu, H., & Zhao, X. (2014). Generating Global LAnd Surface Satellite incident shortwave radiation and photosynthetically active radiation products from multiple satellite data. *Remote Sens. Environ., 152*, 318-332. https://doi.org/10.1016/j.rse.2014.07.003.

Zhang, X., Liu, L., Chen, X., Gao, Y., Xie, S., & Mi, J. (2021). GLC_FCS30: global land-cover product with fine classification system at 30 m using time-series Landsat imagery. *Earth System Science Data, 13* (6), 2753-2776. https://doi.org/10.5194/essd-13-2753-2021.

Zhang, Y., Kong, D., Gan, R., Chiew, F.H.S., McVicar, T.R., Zhang, Q., & Yang, Y. (2019). Coupled estimation of 500 m and 8-day resolution global evapotranspiration and gross primary production in 2002–2017. *Remote Sens. Environ., 222*, 165-182. https://doi.org/10.1016/j.rse.2018.12.031.

Zhang, Y., Peña-Arancibia, J.L., McVicar, T.R., Chiew, F.H.S., Vaze, J., Liu, C., Lu, X., Zheng, H., Wang, Y., Liu, Y.Y., Miralles, D.G., & Pan, M. (2016). Multi-decadal trends in global terrestrial evapotranspiration and its components. *Sci. Rep.-UK, 6* (1). https://doi.org/10.1038/srep19124.

Zhao, H., Montzka, C., Keller, J., Li, F., Vereecken, H., & Hendricks Franssen, H.J. (2025). How Does Assimilating SMAP Soil Moisture Improve Characterization of the Terrestrial Water Cycle in an Integrated Land Surface-Subsurface Model? *Water Resour. Res., 61* (6). https://doi.org/10.1029/2024wr038647.

Zhao, H., Wu, C., & Wang, X. (2022). Large-scale forest conservation and restoration programs significantly contributed to land surface greening in China. *Environ. Res. Lett., 17* (2). https://doi.org/10.1088/1748-9326/ac44c5.

Zhao, X., Liang, S., Liu, S., Yuan, W., Xiao, Z., Liu, Q., Cheng, J., Zhang, X., Tang, H., Zhang, X., Liu, Q., Zhou, G., Xu, S., & Yu, K. (2013). The Global Land Surface Satellite (GLASS) Remote Sensing Data Processing System and Products. *Remote Sens., 5* (5), 2436-2450. https://doi.org/10.3390/rs5052436.

Zheng, C., Jia, L., & Hu, G. (2022). Global land surface evapotranspiration monitoring by ETMonitor model driven by multi-source satellite earth observations. *J. Hydrol, 613*. https://doi.org/10.1016/j.jhydrol.2022.128444.

Zhu, B., Xie, X., Lu, C., Lei, T., Wang, Y., Jia, K., & Yao, Y. (2021). Extensive Evaluation of a Continental-Scale High-Resolution Hydrological Model Using Remote Sensing and Ground-Based Observations. *Remote Sens., 13* (7). https://doi.org/10.3390/rs13071247.